

---

FACHHOCHSCHULE AACHEN, CAMPUS JÜLICH  
Faculty 3: Chemistry and Biotechnology  
European Master of Science in Nuclear Applications (EMiNA)  
Specialisation: Nuclear Technology

---

**Development of a Thermal-Test-Station for  
Target Material Investigations for the Future  
HBS Facilities**

---

*A thesis completed  
at the  
Jülich Centre for Neutron Science (JCNS-2)  
in partial fulfillment of the requirements for the degree of  
Master of Science (M.Sc.)  
at the  
Aachen University of Applied Sciences  
by  
VARUN PAYAK*

*Jülich, October 13, 2019*

1<sup>st</sup> Supervisor:

*Prof. Dr. rer. nat. Karl Ziemons*

2<sup>nd</sup> Supervisor:

*Dr. Paul Zakalek*



# Declaration of Authorship

I, VARUN PAYAK, hereby confirm that this thesis titled, “*Development of a Thermal-Test-Station for Target Material Investigations for the Future HBS Facilities*” has been written by myself, without contributions from any sources other than those cited in the text and acknowledgements.

This applies also to all graphics, drawings, and images included in the thesis.

# Eidesstattliche Erklärung

Hiermit versichere ich, VARUN PAYAK, dass die vorliegende Masterarbeit mit dem Titel “*Development of a Thermal-Test-Station for Target Material Investigations for the Future HBS Facilities*” von mir selbstständig verfasst und angefertigt wurde. Es sind keine anderen als die angegebenen Quellen und Hilfsmittel benutzt worden.

Diese Erklärung erstreckt sich auch auf in der Arbeit enthaltene Graphiken, Zeichnungen und bildliche Darstellungen

# Sperrvermerk

Die vorliegende Masterarbeit basiert auf internen, vertraulichen Daten vom ‘Jülich Centre for Neutron Science (JCNS-2)’ des ‘Forschungszentrums Jülich GmbH (FZJ)’.

Diese Arbeit darf daher nur den Erst- und Zweitprüfern sowie den ermächtigten Mitgliedern der Prüfungsorgane der Hochschule zugänglich gemacht werden. Eine Veröffentlichung und Vervielfältigung der Arbeit ist, auch in Auszügen, nicht gestattet.

Eine Einsichtnahme der Arbeit durch Unbefugte bedarf einer ausdrücklichen Genehmigung durch den Verfasser und das JCNS-2.

Signatures

Place, Date

**Jülich, October 13, 2019**

*“The atoms of our bodies are traceable to stars that manufactured them in their cores and exploded these enriched ingredients across our galaxy, billions of years ago. For this reason, we are biologically connected to every other living thing in the world. We are chemically connected to all molecules on Earth. And we are atomically connected to all atoms in the universe. **We are not figuratively, but literally stardust.**”*

— NEIL DEGRASSE TYSON

# Abstract

The 'Jülich High Brilliance Neutron Source (HBS)' project proposes to develop compact accelerator-driven neutron sources (CANS) via low energy ( $< 100$  MeV) proton induced nuclear reactions ( $p, n$ ) to improve access to neutrons and to counter the shutdown of present low- and medium-flux reactor-based sources. This work serves as a contribution towards developing an in-house experimental thermal-test-station to characterize and investigate the target materials (Be, Al, Steel ... ) under a thermal load as expected from low energetic proton beams ( $\sim 10$  MeV). Although the entire targetry is installed at this setup as per the requirements of the actual CANS systems, the thermal load is, however, generated by low energy electron beams ( $< 10$  keV) to allow for a much easily accessible lab-based experimental workbench. The work is done in two stages: (a) simulations and (b) developmental work. Dedicated ANSYS simulation work towards investigating the thermal and structural conditions reached within the proposed target materials upon impregnation with an electron beam is performed with varying beam power and beam profile. This simulation study is then used as a basis to estimate the operational parameters for initial tests to be conducted at the test station. Corresponding developmental work is done to configure the test-station, including pyrometer calibration, electron gun configuration, electron beam collimation and characterization, and installing the water cooling channel for the target. The simulation results indicate that a gaussian beam profile with twice its standard deviation corresponding to the beam spot radius (15 mm) is an optimum for the employed target geometry, so as to not lose the beam power significantly, while also avoiding structural and thermal failures in the target during operation. However, experimentally achievable beam profile with the available electron gun exhibits a distorted elliptical cross sectional geometry. The optimum working distance with this gun is found to be around 37 mm from the target. At this working distance, the beam has a maximum transversal width of about 25 mm. This work, thus, concludes the setting-up of the experimental thermal-test-station in a functional capacity to conduct first tests, which can then help to validate the simulation work.

# Acknowledgement

Firstly, I would like to thank *Dr. Ulrich Rücker* and *Dr. Thomas Gutberlet* for making it possible for me to work at the Jülich Centre for Neutron Science (JCNS-2), Forschungszentrum Jülich GmbH'. I am profoundly grateful to *Dr. Paul Zakalek* and *Mr. Paul Doege* for accepting to be my supervisors, for guiding me throughout my work, for imparting me with plenty of knowledge and expertise, and for providing sagacious and crucial comments to my thesis to help me actualize this work.

I am immensely appreciative of and thankful to *Prof. Karl Ziemons* for agreeing to be my main supervisor, and for providing me with his valuable time, whenever necessary. His mentorship is pivotal to this work, and it could not have been materialized without his constant support.

My sincere thanks go to *Dr. Johannes Baggermann* for his thorough assistance in the simulation tasks. My special thanks go to *Dr. Jingjing Li* for introducing me to the institute and this field of work. I would also like to thank my dear colleague and friend, *Mr. Marius Rimpler*, who aided me with various potential ideas of configuring the electron gun and provided meaningful suggestions to improve the beam profile.

I would also like to express my warm gratitude to *Mr. Micha Hölzle*, who kindly accommodated me in his office and set up my workstation. I would also like to thank all my other colleagues at JCNS-2, who were always polite and amicable to me, and supported me with my work wherever they could. It made my work at the institute very informative, educational, and most of all really delightful.

Last but not least, I am extremely grateful to my beloved parents, *Mr. Hemant Payak* and *Mrs. Sarita Payak*, my sister, *Ms. Toolika Payak*, and my girlfriend, *Ms Komal Agarwal*, who have always been supportive of me, and have constantly motivated and encouraged me during my work. Their crucial and valuable advice, time and again, has contributed exceptionally to the realization of this work.

# Contents

<b>Abstract</b>	<b>c</b>
<b>Acknowledgement</b>	<b>d</b>
<b>List of Figures</b>	<b>iii</b>
<b>List of Tables</b>	<b>v</b>
<b>1 Introduction</b>	<b>1</b>
1.1 Neutrons and their Applications . . . . .	1
1.2 Neutron Landscape in Europe . . . . .	8
<b>2 The HBS Project</b>	<b>11</b>
2.1 Project Overview . . . . .	11
2.2 Facilities . . . . .	13
2.3 CANS . . . . .	14
<b>3 Theoretical Background</b>	<b>19</b>
3.1 Nuclear Reactions . . . . .	19
3.2 Electrons and their Interactions with Matter . . . . .	25
3.3 Structural Mechanics . . . . .	27
3.4 Thermal Radiation . . . . .	31
<b>4 Simulation</b>	<b>40</b>
4.1 Beam Modelling . . . . .	41
4.2 Simulation Parameters . . . . .	42
4.3 Results and Discussions . . . . .	45
<b>5 Setup of the Target-Test-Station</b>	<b>53</b>
5.1 General Description . . . . .	53
5.2 Pyrometer Calibration . . . . .	55

*CONTENTS*

---

5.3 E-Beam Collimation . . . . .	59
5.4 E-Beam Characterization and Optimization . . . . .	62
<b>6 Conclusions</b>	<b>65</b>
<b>Appendix: 1</b>	<b>A 1</b>
<b>Appendix: 2</b>	<b>A 3</b>
<b>Appendix: 3</b>	<b>A 7</b>
<b>Bibliography</b>	<b>B 1</b>

# List of Figures

1.1	Neutron Structure . . . . .	2
1.2	Comparison of Probes: Electrons, Neutrons, and Photons . . . . .	4
1.3	Comparison of Probes: X-Ray and Neutron Coherent Cross Sections . . . . .	4
1.4	Future Neutron Sources Scenario . . . . .	9
2.1	Future Neutron Sources Scenario . . . . .	11
2.2	The Large HBS Facility . . . . .	13
2.3	The Small NOVA ERA Facility . . . . .	14
2.4	Target Geometry NOVA ERA . . . . .	17
3.1	Nuclear Reaction Mechanisms . . . . .	22
3.2	Neutron Production Cross Sections for Protons in Be . . . . .	24
3.3	Neutron Production Cross Sections for Deuterons in Be . . . . .	24
3.4	Thermal Radiation and IR Transmittance . . . . .	32
3.5	Blackbody Spectrum . . . . .	35
4.1	2D Gaussian Heat Flux Profile . . . . .	42
4.2	Simulation Setup . . . . .	43
4.3	Physical Constraints on the Geometry . . . . .	44
4.1	Simulation Results: Plots (0-5 kW) . . . . .	48
4.2	Simulation Results: Plots (0-1 kW) . . . . .	49
4.3	Simulation Results: ANSYS Graphics . . . . .	51
4.4	Material Comparison . . . . .	52
5.1	Thermal Target Test Station . . . . .	53
5.2	PYROSPOT DPE 10M . . . . .	55
5.3	Emissivity Curves . . . . .	56
5.4	Pyrometer Calibration Setup . . . . .	58
5.5	Pyrometer Calibration Curves . . . . .	58

*CONTENTS*

---

5.6	Beam Profile Measurement . . . . .	60
5.7	Electrodes' Effects on E-Beam Profile . . . . .	61
5.8	Final E-Gun Configuration . . . . .	62
5.9	Beam Profile Characterization . . . . .	63
5.10	Beam Area vs Distance . . . . .	64
A3.1	Beam Profile Curves . . . . .	A 8
A3.2	Photographed Beam Spots . . . . .	A 9

# List of Tables

1.1	Element Properties . . . . .	2
2.1	Material Thicknesses . . . . .	16
3.1	Nuclear Reactions for Monoenergetic Neutrons . . . . .	23
3.2	Kanaya–Okayama Range . . . . .	27
4.1	Maximum Permissible Power . . . . .	45
4.2	Simulation Results . . . . .	50
5.1	Pyrometer Technical Specifications . . . . .	55
A1.1	Beryllium Material Properties . . . . .	A 1
A1.2	Aluminium Material Properties . . . . .	A 1
A1.3	Steel Material Properties . . . . .	A 2
A2.4	2D Gaussian Expectation Values . . . . .	A 6

*Dedicated to my Late Grandfather, **Prof. Dr. M. M. Payak,**  
Mycologist and Plant Pathologist  
(1928-2010) ...*

# Chapter 1

---

## Introduction

---

The foremost intention of this work is to contribute to the development of an experimental setup to investigate and study the behaviour of various target materials under the impact of thermal loads, generated by charged particle beams (protons or deuterons), as part of the *Jülich High Brilliance Neutron Source (HBS) project* (see Section 2 on page 11). The experimental setup, hereafter referred to as *test station*, will employ a correlating approach of approximating these thermal loads using a low energy ( $< 10$  keV) electron beam. While this distinctly stands out as being of crucial importance and the main objective of this research work, it is also noteworthy to outline the general impetus behind this work: the advent need to procure a solution to counterpoise the prognosticated paucity of low- and medium-flux neutron sources in the near future, especially in Europe [1].

This issue has been identified and is being addressed by a team of researchers at the Jülich Centre for Neutron Science (JCNS) of the Jülich Research Centre, which includes the development, establishment, and successful operation of accelerator-based neutron facilities with scalable energy and intensity regimes to allow easy access of neutrons to users and to further strengthen the neutron science and innovation in Europe. [2, 3]

### 1.1 Neutrons and their Applications

To fathom the extent of usability of neutrons, it is absolutely vital to have a basic understanding of the neutron itself. Figure 1.1 on the next page shows the basic structure of a neutron as a composite particle, consisting of three different quarks (1 up and 2 down, *udd*). Neutrons are, thus, baryonic particles that have no electrical

charge. As opposed to protons, neutrons are not stable in an unbound state. A free neutron decays via a  $\beta^-$ -emission into a proton, an electron, and an electron antineutrino, with a mean life-time of about 882 s. Table 1.1 summarizes some of the important properties of a neutron.

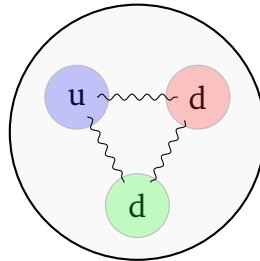


Figure 1.1: Structure of a neutron. [4]

Table 1.1: Properties of a neutron in comparison to protons and electrons. [5, 6]

Particle	Properties					
	Mass	Charge	Radius	Spin	MDM <sup>a</sup>	EDM <sup>b, c</sup>
	[u]	[e]	[m]	[ $\hbar$ ]	[ $\mu_N$ ]	[e cm]
e	0.000549	-1	$\sim 10^{-18}$	1/2	$\sim 1836$	$8.7 \cdot 10^{-29}$
p	1.007276	+1	$\sim 10^{-15}$	1/2	2.79	$5.4 \cdot 10^{-24}$
n	1.008664	0	$\sim 10^{-15}$	1/2	-1.93	$2.9 \cdot 10^{-26}$

a - Magnetic dipole moment      b - Electric dipole moment      c - Experimental upper limit

Even though free neutrons decay, their mean life-time is long enough for most applications. Owing to their charge neutrality, these particle are also not subjected to Coulomb potentials, and thus, can penetrate deep into matter, without ever being obstructed by the much lighter electrons, as shown in Table 1.1. In addition, neutrons are the most easily accessible neutral spin half systems that participate in all the four known fundamental interactions.

Neutrons, therefore, serve as a profoundly essential scientific tool to probe structural, magnetic, and dynamic properties of matter within a huge array of length and time scales, ranging from sub-nuclear domains to macroscopic objects

and from a few femtoseconds to a few seconds. This renders them as ideal probes for a multitude of applications, both in research and industry, especially those that are of distinguished interest to the field of condensed matter science by means of neutron scattering experiments.

Evidently so, neutrons also offer a broad-ranging spectrum of applications to other science disciplines. Neutron-induced nuclear reactions are also pivotal to some of the most advanced and multidisciplinary research fields, such as nuclear astrophysics, dosimetry, radiopharmacy, radioisotope production, energy production, space science, nuclear waste transmutation, non-invasive scanning techniques, etc. [7].

### 1.1.1 Neutron Scattering

Scattering, by definition, means the process in which radiation or particles are deflected by any obstructing medium in their path of propagation. It is a powerful means of studying local microscopic effects and phenomena in matter, which helps us to build models about the collective emergent physical properties at macroscopic scales. Scattering data, however, reveals information intrinsically in the *reciprocal space*, which requires analysis to correlate it to the *real space*.

Understandably so, neutron scattering is a technique to intentionally scatter neutrons off a given target material, and analyzing the scattered neutrons to elucidate the intricate structure and dynamics of the given material. There are, of course, other radiation and particle sources that can be used to conduct scattering experiments, such as X-rays, synchrotron radiation, electrons, atomic beams, etc, due to their strong interaction with matter. However, neutrons offer a certain advantage over the others.

As is evident from Figure 1.2 on the following page, neutrons' wavelengths at far lower energies (in the order of a few meV) already correspond to the atomic distances. This, however, is not the case with photons or electrons. They need much higher energies, in comparison to neutrons, to be at similar wavelengths. This, while not always a problem, does pose serious challenges to investigate sensitive and delicate biological samples, such as proteins, DNA samples, etc. Higher probe energy also means higher imparted energy to the sample. This may ruin the sample, and thus, softer radiation might be the only optimum choice.

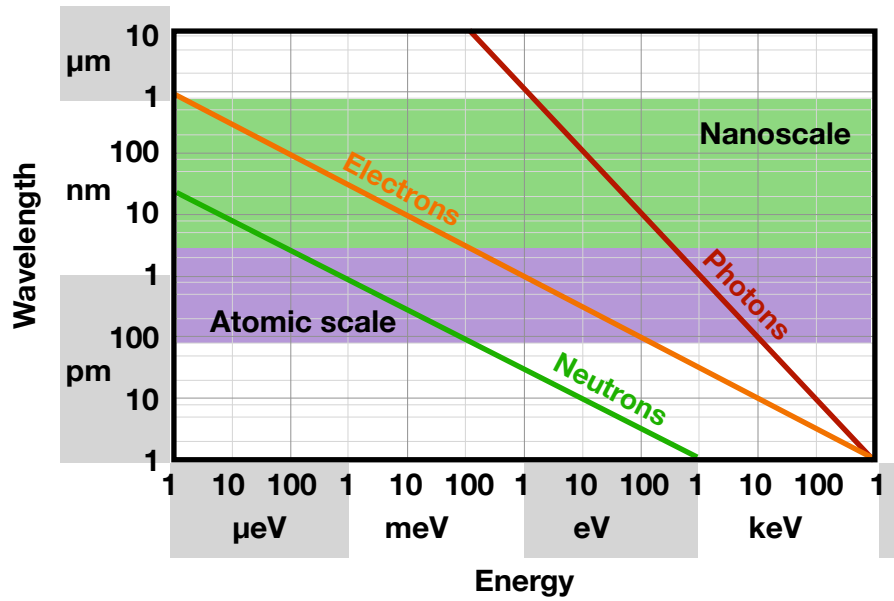


Figure 1.2: Comparison of the three probes—neutrons, electrons, and photons—in a double logarithmic energy-wavelength diagram. [8]

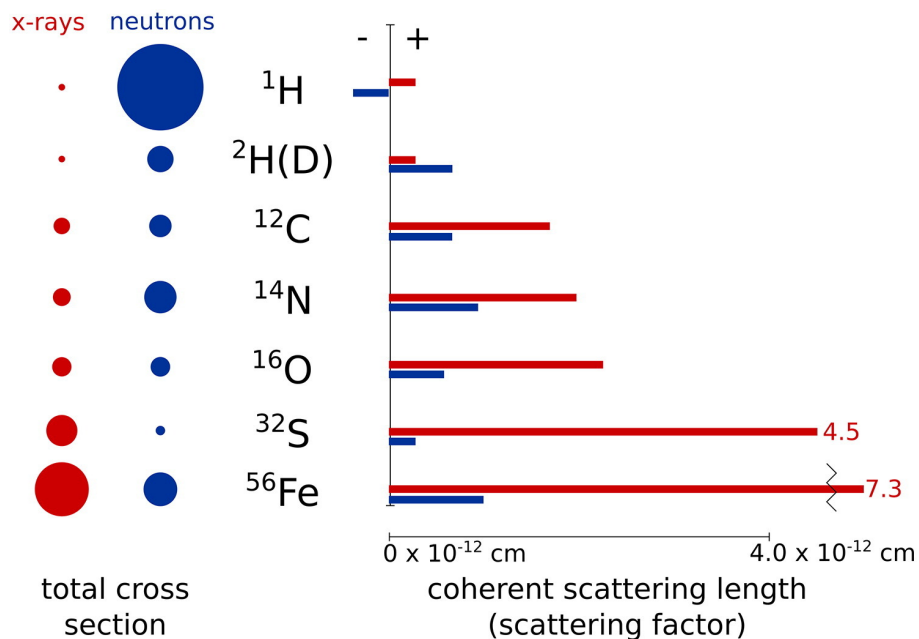


Figure 1.3: Comparison of the coherent scattering cross sections for X-rays and neutrons for a selection of elements. [9]

Moreover, since photons and neutrons interact differently with matter—photons interact with the electron cloud of atoms, whereas neutrons with the atomic nu-

clei—it is important to know *a priori* about the structural composition of the sample, before carrying out the experiments. So, for instance, hydrogen position determination with X-rays, especially in the presence of other heavier elements, will be difficult, since X-ray photons would yield a stronger signal for heavier elements, overshadowing the response from hydrogen atoms. Besides, neighbouring elements of the periodic table and isotopes are nearly impossible to distinguish from one another via X-ray scattering techniques, since there will be no contrast between the signals. With neutrons this is not the case, for their cross sections depend on the nuclear structure of the respective atomic nuclei. Thus, there can be a huge difference in the cross sections even amongst different isotopic species of the same element, e.g. hydrogen and deuterium. Figure 1.3 on the previous page highlights this difference comprehensively for a selection of elements.

In all fairness, neutron scattering techniques reveal crucial information about matter, but it is still not a complete package. Often other techniques are employed, complementary to neutron scattering, to derive a deeper and more accurate understanding of the microscopic world.

### 1.1.2 Neutron Imaging

In contrast to scattering, imaging is a method to probe structures in *real space* and usually corresponds to macroscopic objects. Neutron imaging is helpful as a complementary tool to X-ray imaging. Since X-rays interact with the electron cloud of atoms, it is difficult to image objects shielded by heavy elements such as lead. Neutrons travel almost unhindered through lead, and thus, can reveal information about even shielded structures. Moreover, modern day digital recording of data has made it possible to render even 3D tomographic volumes. In addition to this, it is mostly done via fast neutrons, which means often compact neutron sources can be employed without moderation steps, enhancing the usable flux portion of any given source. [10]

### 1.1.3 Elemental Analysis

Neutrons are a unique probe not only for scattering and imaging, but also for detecting trace amounts of elements in a given sample by means of neutron activation analysis (NAA) and prompt-gamma neutron activation analysis (PGANN). The former is an offline technique, meaning the sample is first irradiated with a

thermalized neutron flux and then taken out for analysis, where the decay products in the sample are analyzed. PGNAA, however, is an online technique, wherein the gammas from the radiative neutron capture reactions within the sample are analyzed. The gamma peaks are characteristic to individual elements, and thus, deliver information about the composition of the sample. Fast and highly efficient gamma detectors make PGNAA an instrumental tool for mining industries, to scope for minerals of interest. [11]

### 1.1.4 Radioisotope Production

Neutrons play a vital role in providing radioactive isotopes of medical importance and have led to great strides in the areas of diagnostic and therapeutic nuclear medicine. Most production routes require high neutron-flux to gain optimum specific activities of the sought after products. In essence, this means that a majority fraction of these radioisotopes are produced in a nuclear reactor with typical fluxes of  $10^{14}$  n/cm<sup>2</sup>/s to a few  $10^{15}$  n/cm<sup>2</sup>/s [12].

#### 1.1.4.1 Fission Based

The medical radioisotope, <sup>99</sup>Mo, is predominantly produced by processing neutron-irradiated uranium based targets in high flux reactors, as one of the main fission products. <sup>99</sup>Mo decays into its daughter <sup>99m</sup>Tc, which is used in ca. 85 % of all nuclear medicine, imaging, and diagnostic procedures globally. As a consequence, <sup>99m</sup>Tc is also known as the workhorse isotope of nuclear medicine [13, 14]. Similarly, for therapeutic radioisotope <sup>131</sup>I, and SPECT relevant <sup>133</sup>Xe, the ideal routes of production are also fissioning of uranium by neutrons. [12]

#### 1.1.4.2 Neutron Capture Based

Several other radioisotopes of interest are produced via neutron capture reactions. <sup>186</sup>Re, obtained via irradiating enriched <sup>185</sup>Re with neutrons, can even be used with low specific activities for palliative treatment against bone pains. Many others such as <sup>177</sup>Lu, <sup>153</sup>Sm, etc. are also procured via capture reactions with distinctly high specific activities [15].

#### 1.1.4.3 (n,p)-Based

Another intriguing and popular way of producing radioisotopes, mainly for light mass species, is via (n, p) reactions. The advantage of using this route is primar-

ily based on its simple methodology and high specific activities of the obtained radioisotopes. Commonly produced therapeutic radionuclides include  $^{32}\text{P}$  and  $^{67}\text{Cu}$ .

### 1.1.5 Boron Neutron Capture Therapy (BNCT)

Neutron-induced nuclear reactions are crucial in the treatment of cancer via BNCT. Boronated compounds, such as BPA (para-borono-phenyl-alanine) are introduced in the body at tumor-ridden locations. The organ is then externally irradiated with thermal neutrons, which initiates a cascade of  $(n, \alpha)$  reactions. The released  $^4\text{He}$  and  $^7\text{Li}$  charged particles then contribute to the therapeutic effects at the cancer site. [16]

### 1.1.6 Power Generation

One of the most applied field of neutrons' utilization is in power production, currently via nuclear fission reactors, which amounts to about 15 % of world's total electricity production [17]. Neutrons are the key driving force behind a successful controlled fission reactor. Since each fission releases about 2-3 neutrons on average (in case of  $^{235}\text{U}$ ), it is possible to steer a self-sustaining chain reaction, wherein only one neutron is effectively used per fission to induce another fission event. This releases a huge amount of energy in the process, which is used eventually to generate electricity.

A collective global effort is now being put into the development of a commercially viable nuclear fusion power plant, which would be energy-wise cleaner, more efficient, and reliable [18, 19].

### 1.1.7 Nuclear Astrophysics

A fundamental challenge in nuclear astrophysics is deciphering the origin, synthesis, and abundance of the existing chemical elements and their isotopes. Even though, it is now well known that origin of nuclei up to the Fe–Ni region occurs in the core of massive stars through various fusion reactions, the early stage birth of the lighter elements that fuel the stars (isotopes of H, He, and Li) were created by primordial nucleosynthesis shortly after the Big Bang [7, 20] through neutron reactions. Neutron reactions also contribute to the production of almost all heavier nuclei beyond Fe. These neutron rich elements are typically formed in the later phases of stellar evolution amidst the He and C burning cycles [7, 21, 22], in the

extinction events of massive stars via supernova explosions [7, 21, 23], and in the coalescence of neutron stars in a binary system [7, 24]. In all scenarios, the principal neutron reactions that dictate are the sequential slow (*s*) and/or rapid (*r*) neutron capture reactions ( $n, \gamma$ ), which renders studying neutron capture reactions of utmost importance [22, 24].

## 1.2 Neutron Landscape in Europe

For most applications, moderate to high fluxes of neutrons are required [25]. These are typically offered by large-scale user facilities that operate either on reactor-based continuous neutron beams or pulsed neutron beams in spallation sources. In any case, construction, commissioning, and proper operation of such a facility is an expensive and challenging endeavour. This already puts a limit on the number of such facilities available worldwide.

It is foreseeable that a lot of reactor-based facilities will shut down globally and in particular in Europe, owing to their remaining ephemeral lifetime and changes in the political policies. Figure 1.4 on the following page depicts a predicted overview of developments in Europe, concerning the neutron user facilities. The Berlin (BER II) and Saclay (ORPHEE) reactors are expecting their shutdown by the end of 2020. In Europe, this would create a first major drop in the instrument beam-days<sup>1</sup>. A second major drop would soon follow in the years 2023-2024, after the scheduled end of operational licenses of the Budapest (BRR), REZ (LVR-15), and ILL facilities. This scenario is predicted to change with the commissioning of the European Spallation Source (ESS). However, this too would take some years until its full capacity is reached, in terms of accelerator power, instrumentation, etc. Consequently, there is an anticipated shortage of available neutron sources, and while a grand facility such as ESS is planned to come into effect, the process is piecemeal and cannot fully compensate for the lack of several others [1].

Even with facilities such as ESS, the opportunities of neutron science will be accessible only to adept and advanced users. Thus, an alarming increase in the demand of low- and medium-flux neutron sources is directly identifiable, especially

---

<sup>1</sup>Instrument beam-days is used in the context of quantifying the overall capacity and capability of a neutron user facility to better assess the size of the user community that can be sustained by it.

those that are aimed towards method and instrument development, education and training, etc.

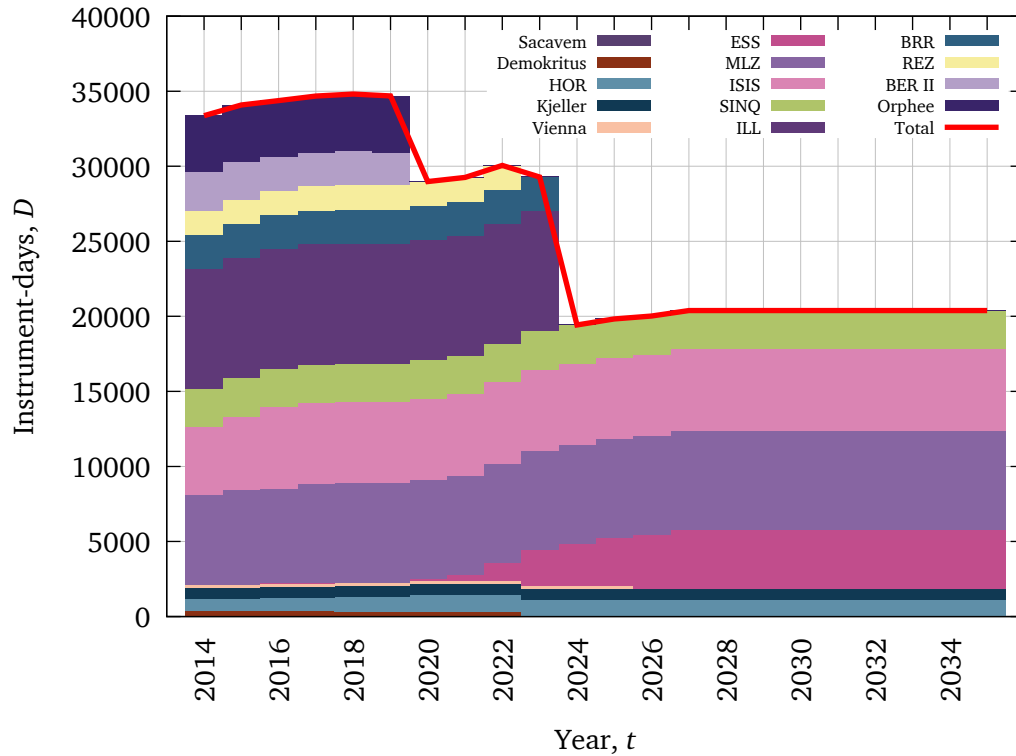


Figure 1.4: Future Neutron Sources Scenario [1].

As alluded, more neutron user facilities are needed, in order to further the ongoing development of neutron science, innovate novel technologies, and push the bracket of education and training for the less experienced and industrial users by means of smaller sources. This is where the HBS project steps in, aiming to develop scalable accelerator driven neutron sources to better the forecasted scenario (see Chapter 2 on page 11 ).

Due to their bound state in matter, extracting neutrons, in most cases, demand some or the other nuclear reactions, which are often endoergic<sup>2</sup>. Even though numerous nuclear reactions and processes that are well understood can contribute to the production of neutrons, serious experiment-driven considerations have to be made before opting any particular type of reaction [26], which limits the actual

<sup>2</sup>Endoergic reactions are reactions that take up a certain amount of energy to occur.

exploitable approaches. One such meritorious reaction path is via low energy proton (or deuteron) induced nuclear reactions (see Section [3.1.3 on page 23](#)), which will be the *modus operandi* of the HBS project.

## Chapter 2

# The HBS Project

### 2.1 Project Overview

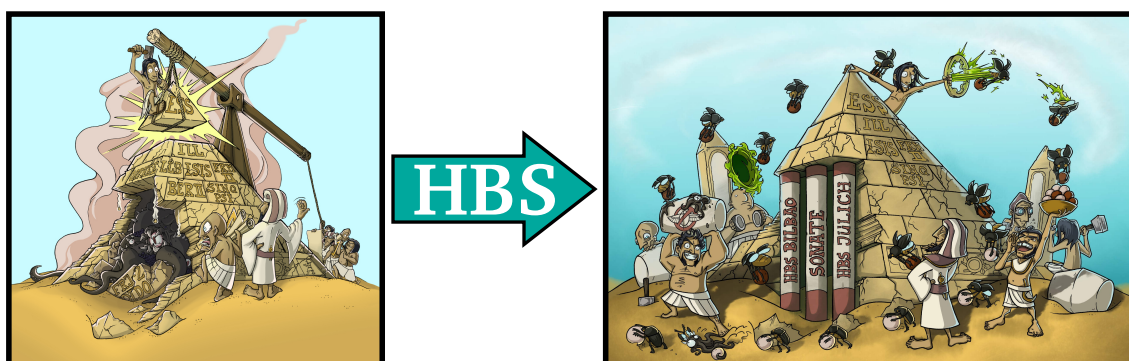


Figure 2.1: Future Neutron Sources Scenario [27, 28].

In the light of Section 1.2, it is discernible that small to medium flux neutron sources targeted towards education, method development, proof-of-principle experiments, etc. may come to a standstill in the near future. The JCNS led HBS project is an initiative to respond to this scenario, which can be best represented pictorially in Figure 2.1. The pyramidal depiction of the present scenario highlights the fact that numerous user facilities are going to phase out, thereby weakening the neutron user community at its base. This must, therefore, be compensated by new facilities, which is where the HBS project comes into play, strengthening and supporting the neutron science by delivering a compact and cost-efficient neutron production system.

Unfortunately, the shutting down of these facilities do not yet have any replacement plans. This is primarily because of the fact that all these facilities are research reactors, and while research reactors are nowhere nearly as cumbersome as power plants, their operation is, nevertheless, fraught with a lot of problems. This is also evident in the complicated nuclear licensing procedures required to construct and operate such a facility. Thus, it seems highly improbable that the future neutron sources in Europe, and especially in Germany, will be reactor-based. Consequently, alternatives are being explored, one of which is to produce neutrons via accelerators.

One such concept is proposed by the HBS project: to develop scalable compact accelerator-driven neutron sources (CANSs) with high brilliance<sup>1</sup>, optimized for neutron scattering and analytics. Such a source produces neutrons mainly via low energy ( $< 100$  MeV) proton (or deuteron) induced nuclear reactions, e.g.  $X(p, n)Y$ , in suitable target materials (Be, V, Ta, etc.). The usual efficiency of such a process is around  $10^{-2}$ - $10^{-1}$   $n/p$  (or  $n/d$ ).

At first, this seems exceedingly inefficacious compared with the state-of-the-art spallation neutron sources, which produce almost 3 orders of magnitude more neutrons per proton ( $\sim 20$ - $30$   $n/p$ ) with significantly less heat release per neutron. However, spallation sources operate typically in GeV regimes, requiring sophisticated accelerators with heavy shielding and considerably large space. This makes the whole setup incredibly expensive. A CANS, on the other hand, operating at much lower energies avoids these issues, and thus, allows for a much compact installation overall. Each integral component of such a machinery, ranging from an ion source to extraction channels for neutrons, can be optimally designed and enhanced, enabling the entire system to become more space-economic as well as competitive with other sources. [3, 30]

While conventional neutron sources are optimized to provide the highest deliverable integral neutron flux, the HBS project aims at optimizing the brilliance of a neutron beam specifically tailored to suit the needs of a particular experiment. The

---

<sup>1</sup>Brilliance can be understood as ‘spectral brightness’ of a source (neutron or photon), which is defined as the intensity per unit time, source size, and divergence over a given spectral bandwidth. Conventionally, this is expressed as:

$$B = \frac{\text{neutrons}}{\text{s} \cdot \text{cm}^2 \cdot \text{mrad}^2 \cdot 0.1\% \frac{\Delta\lambda}{\lambda}} \cdot [29]$$

reason behind maximizing the beam-brilliance is to be able to conduct statistically successful scattering experiments with very small samples, such as small protein single crystals, magnetic nanoparticles, etc. [3]

## 2.2 Facilities

As mentioned in the previous section, these CANSs are conceptualized to be scalable systems. This means that the energy and intensity regimes are variable and can range from a low-power source ( $P_{av} \sim 1$  kW at the target) to a high-power source ( $P_{av} \sim 100$  kW at the target). The low-power source has been named as NOVA ERA (short for Neutrons Obtained Via Accelerators for Education and Research Activities [31]) and is aimed at basic research and training experiments, whereas the larger HBS facility will serve as a national user facility, occupying its position at the forefront of advanced neutron science. Both the sources will be operated as pulsed sources, depending on the duty cycle of the corresponding accelerator systems. [30]

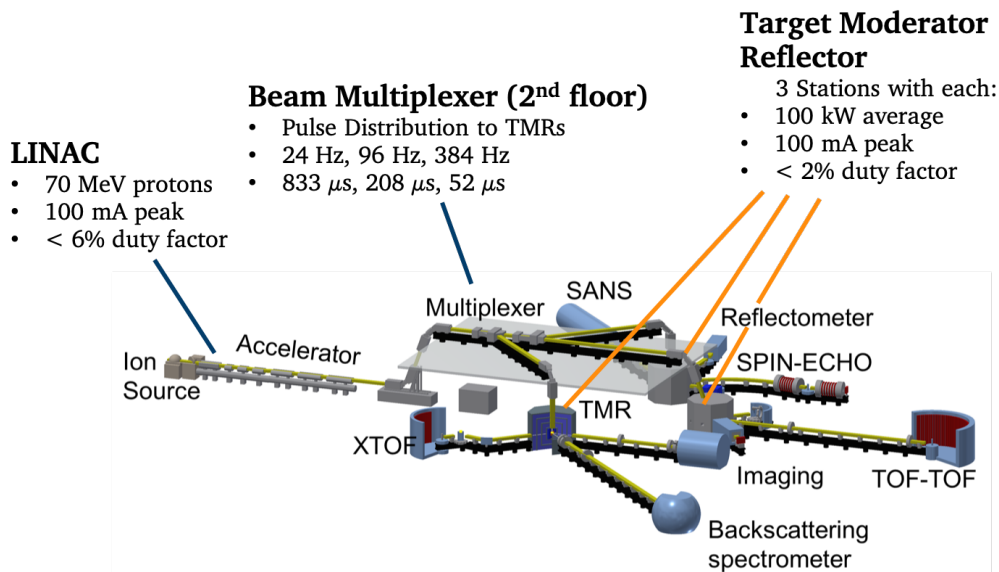


Figure 2.2: The high power HBS facility along with its various components and subsystems.

### 2.2.1 The Large HBS Facility

The station, as illustrated in Figure 2.2, will employ a 70 MeV pulsed proton beam with a duty cycle of  $\sim 2\%$  on heavy targets (such as Tantalum), amounting to an

average heat load of 100 kW in the target. With such a setup, an average neutron source strength of about  $5 \cdot 10^{14}$  n/s can be achieved [30, 31].

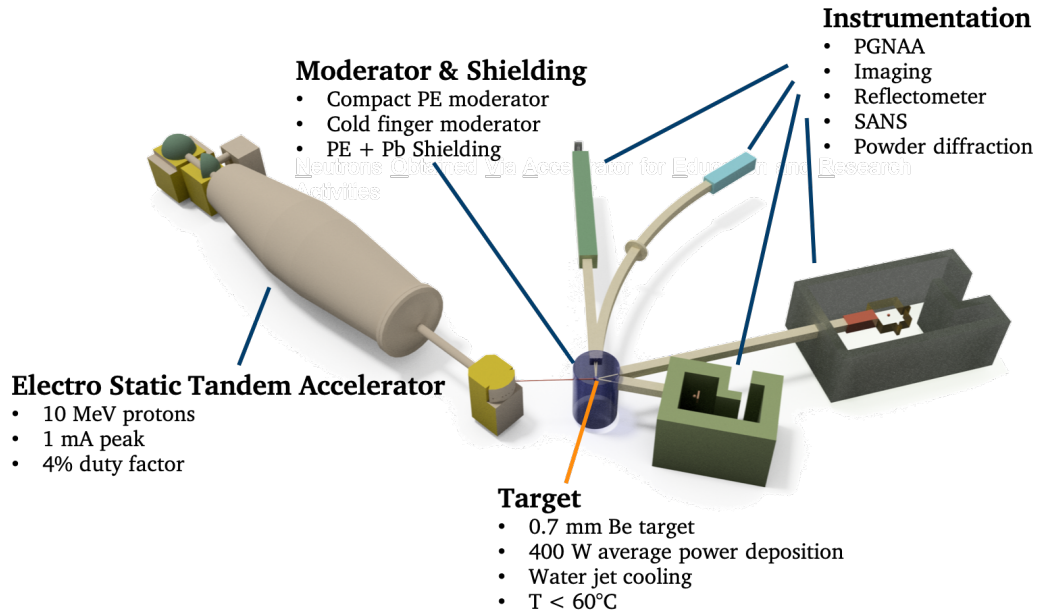


Figure 2.3: The low power HBS facility, also named *NOVA ERA*, along with its various components and subsystems.

## 2.2.2 NOVA ERA

The term NOVA ERA stands for Neutrons Obtained Via Accelerators for Educational and Research Activities. This station, as illustrated in Figure 2.3, will employ a 10 MeV pulsed proton beam with a duty cycle of 4% on light targets (such as Beryllium). Under such a setup and with a proton beam at a peak current of 1 mA, the target is subject to an average ion beam power of 0.4 kW. With Beryllium targets, an average neutron source strength of about  $3 \cdot 10^{11}$  n/s can be obtained [30, 31].

## 2.3 CANS

The progress and evolution of the high power accelerator technology, detection efficiency and resolving capabilities of particle detectors, and abilities to model the neutronics of large, complex systems in the recent decades have all coherently contributed to the development and advancement of an emergent new domain of accelerator-driven systems (ADS). The technology exploits the inherently safer and

controllable particle accelerators to steer systems that operate in important areas such as production of medical radioisotopes, tritium production, nuclear waste transmutation, neutron production, etc. [32]

Even though neutron sources at research reactors have provided deep insight into the advanced applications of neutrons, setting up a sophisticated experiment at such reactors and is cumbersome and costly. But the main disadvantage with these reactors is that their core cannot be easily switched on and off at one's disposal. Thus, the flexibility in terms of control is highly limited. ADS are, on the other hand, turn-key systems, making them highly suitable and attractive for industry as well as research. [33]

Since accelerators can be made smaller and more compact, special relevance is being drawn towards systems that are coupled with such small and medium power accelerators, with power levels ranging between a few kW to hundreds of kW. Thus, electrostatic tandem accelerators, cyclotrons, linear accelerators, etc. can be coupled with proper targetry to generate neutrons, mostly via (p, n) and (d, n) reactions [33]. Such a system with dedicated and compact target-moderator geometry that exploits low energy nuclear reactions to produce neutrons are called compact accelerator-driven neutron sources or CANS.

### 2.3.1 Components

A CANS, in general, has several integral elements and components, ranging from an ion source to extraction channels for neutrons. The above stated facilities will each consist of an accelerator station, one or multiple TMR (Target-Moderator-Reflector) setups, and neutron optics and dedicated instruments, as illustrated in Figures 2.2 on page 13 and 2.3 on the previous page. The TMR includes a target, a thermal (and cryogenic) moderator, and a suitable shielding for gammas and neutrons. Each of these components have to be selected and tailored to optimize the neutron brilliance, and to simultaneously attain a reliable and robust compact geometry. This already puts numerous constraints on every part of such a powerful CANS, with the target being no exception [31].

For obtaining a high brilliance, two major considerations are necessary. Firstly, the target has to be small and dense, and secondly, it should be exposed to a high ion beam current. It is, therefore, evident that the target is subject to a high

deposited power density ( $\sim 1 \text{ kW/cm}^2$  for the large facility) [34].

### 2.3.2 Target

For the purposes of this work, the target geometry for the NOVA ERA facility has been chosen, which is susceptible to an incident 10 MeV proton beam. The target material must consequently fulfill certain pre-requisites. On the one hand, it should provide sufficient mechanical stability to withstand the thermal stresses generated by  $\text{H}^+$ -ion depositions, and on the other hand it should be able to avoid blistering issues and account for a high hydrogen diffusion coefficient or high hydrogen retention properties [35].

A preferred material in this case is Beryllium, since it has a high neutron yield at lower proton energies ( $< 20 \text{ MeV}$ ) and also exhibits good mechanical and thermal properties (see Appendix 6). The other two selected light target materials for the employed beam energy are Aluminium and Steel. Although the neutron yield for Aluminium and Steel is much lower compared to Beryllium, their mechanical and thermal properties provide for better structural strength and robustness (see Appendix 6).

Table 2.1: Calculated thicknesses for given materials using TRIM for an incident 10 MeV  $\text{p}^+$  beam, exiting the target with 2 MeV.

Material	Thickness, $t$
	[mm]
Steel	0.235
Aluminium	0.581
Beryllium	0.700

The thickness of the respective materials is based on (i) the range of the protons in the target materials and (ii) the premise that the exiting proton beam should have an energy of 2 MeV. The 2 MeV beam energy at the exit results from the energy threshold for the  ${}^9\text{Be}(p, X)n$  reaction [36], which is then considered for all the cases. As a result, most ions that go unreacted through the target material do not get deposited in the target, thereby reducing the accumulation of  $\text{H}^+$ -ion

deposition over the time of operation. The beam is, thus, suggested to be dumped in the coolant water itself. The target thicknesses have been determined using the TRIM tool [37] as shown in Table 2.1.

Figure 2.4 shows the sectioned view of the simplified target design for the NOVA ERA facility, wherein the target is a thin disc of diameter 80 mm and appropriate thickness (see Table 2.1). The exposed target area to the incoming beam is a circular region of diameter 40 mm (corresponding to that of the accelerator beam tube). In order to avoid the beam hitting the target housing, the beam spot is set to an optimized diameter of 30 mm [36]. The target sits between the two flanges, and the coolant water is pumped to the back side of the target disc, which is then led out through 11 exit holes arranged in a circular array. Preliminary experimental data and simulations with this configuration have shown that an estimated neutron yield of  $(2.1 \pm 1.1) \cdot 10^{13} \text{ s}^{-1} \text{ mA}^{-1}$  can be achieved with a 10 MeV proton beam on a Be target ( $\phi = 80 \text{ mm}$ ,  $t = 0.7 \text{ mm}$ ) [31].

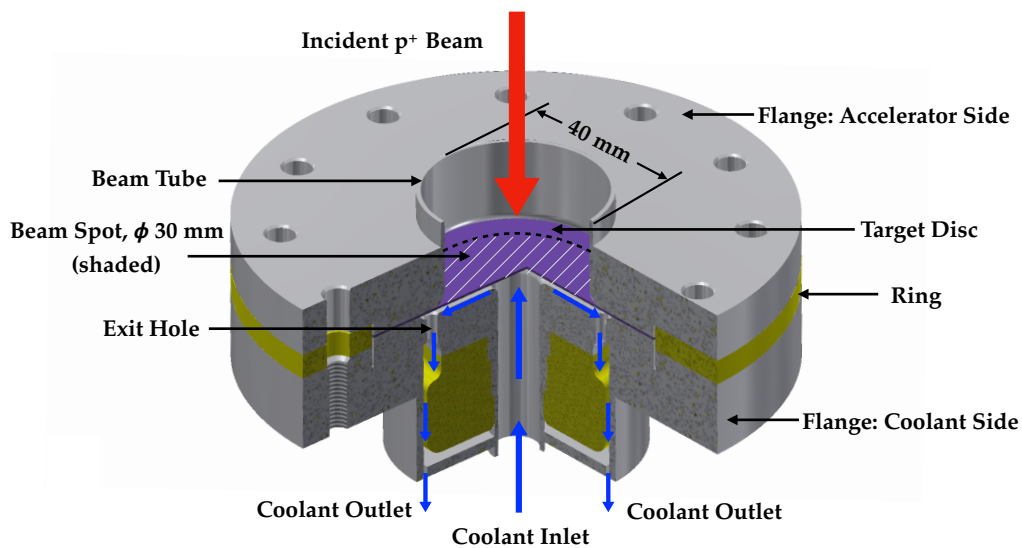


Figure 2.4: Sectioned view of the simplified target assembly for the NOVA ERA facility.

To carry out these thermal test studies with a proton beam is, however, not always feasible, since a proton accelerator with the required beam current and energy is not always accessible. Thus, an alternative approach to conduct these experiments was proposed, which involves a much simpler setup of testing the target materials with an electron beam irradiation instead. This has the advantage

of using a simple thermionic electron gun, which is for many practical reasons, easy to handle and operate, and does not pose serious shielding issues.

# Theoretical Background

---

## 3.1 Nuclear Reactions

### 3.1.1 Introduction

The modern subject of nuclear reactions is a well-versed and highly investigated area of research. Not only has there been an enormous push to study these processes, but also a collective global effort to document all experimental and evaluated data for advanced nuclear science and applications in form of structured libraries, accessible to people involved in all spheres of research and development. [38–41]

Of particular relevance are the nuclear reactions below 100 MeV, since these predominantly contribute to the development and production of radionuclides that are of immense medical importance [42]. More so, at these low energies, individual nucleons (protons and neutrons) involved in the reactions are conserved (not the case above 140 MeV). As a result, nuclear reactions within this energy regime are far better understood via well known models [41].

### 3.1.2 Nuclear Reaction Mechanisms

To understand and make elaborate use of these reactions, it is necessary to have a thorough knowledge of their intrinsic mechanisms. For the sake of simplicity, only reactions involving two nuclear species shall be discussed in detail.

When two or more atomic nuclei or subatomic particles (protons, neutrons, electrons, etc.) approach one another to extremely close distances (of the order of a few fm), these particles may exhibit a variety of processes. In cases, where the interacting particles adhere to their original identities, they are said to have undergone (nuclear) scattering processes. In cases, where the interacting particles are, however, transformed, into a completely new set of particles, they are said to have undergone nuclear reactions. [43]

Undeniably, all atomic nuclei and most subatomic particles possess some quantifiable electrical charge. This essentially means that the interaction of any two given nuclear species is subjected to the Coulomb potential barrier, when of similar charges. Exceptions exist in cases, where at least one of the two interacting nuclear species is electrically neutral, such as a neutron ( $n$ ), a neutrino ( $\nu$ ), a photon ( $\gamma$ ), etc.

Consequently, nuclear reactions comprising of charged species are only feasible, when the interacting species have acquired sufficient energy to overcome the Coulomb threshold. In nature, such reactions often occur in the earth's atmosphere, where the cosmic particles with colossal energies are continuously showering from the outer space. In laboratories, the threshold energy level is often achieved via external means, such as particle accelerators, natural or artificially produced radioactive sources ( $\alpha$ -emitting  $^{241}\text{Am}$ ), etc. [41]

Oftentimes, this is accomplished by impinging one of the particles (projectile) onto the other (target). The target is usually at rest, in the laboratory frame of reference, and the projectile is brought to the relevant energy values. A nuclear reaction, thus, yields particles that are ejected out of the target (ejectiles), leaving behind the transformed nuclei mostly within the target (products). Contrary to chemical reactions, the reaction products are not deterministic in nature. Nuclear reactions are stochastic quantum processes, and the outcome of any nuclear interaction can be only described as a set of statistical probabilities of many possible outcomes, each being referred to as a *reaction channel*. The probability of a particular reaction channel to come into existence is defined by the projectile particle energy and the corresponding reaction cross section. [41, 44]

A typical low-energy nuclear reaction can be characterized by the following parameters:

- i Q-value;
- ii energy threshold;
- iii reaction cross section;
- iv energy and angular distribution of the ejectiles;
- v differential and integral data; and
- vi excitation function.

Nuclear reactions can be well explained in terms of several reaction mechanism models that describe and characterize the various kinds of nuclear processes, occurring during the temporal evolution of the intermediate states achieved in a reaction [44]. In general, for interactions of light mass projectiles with target nuclei, the reaction mechanisms can be classified into three main categories:

- **Compound nucleus formation and decay**

At low energies, incident projectile particles can be captured by target nuclei, coalescing to form an excited state compound quantum system. The system loses all information prior to the formation of this compound state, and the excess energy is homogeneously distributed throughout the nucleus, which then subsequently de-excites, in one or more steps, via particle(s) emission (or evaporation). Therefore, the probability of the de-excitation depends only on the energy, angular momentum, and parity<sup>1</sup> of the quantum state of the compound nucleus. The usual time scale for this process is  $\tau \sim 10^{-15}$  s. Due to the homogenized energy spread, the particle emission is usually isotropic. [41, 44]

- **Direct reaction**

This typically describes reactions that occur without any intermediate state, i.e., the projectile and the target nucleus interact for a much shorter time duration,  $\tau \sim 10^{-21}$  s, such that mostly only a possible exchange of particles or energy can happen between them. In case of a particle exchange, either a nucleon is stripped off from the projectile and is transferred to the target or vice versa. The former is known as a **stripping reaction**, and the latter is known as a **pick-up reaction**. If, however, only energy is exchanged, it becomes **inelastic scattering**. These reactions, thus, are favourably forward

---

<sup>1</sup>In quantum mechanics, parity represents the property of a quantum state to exhibit chirality under a mirror transformation (or parity transformation). Thus, phenomena that are not symmetric under a parity transformation are chiral in nature, such as the weak interaction.

peaked, meaning that the direction of ejectiles is mostly in the direction of the projectiles. [41, 44]

- **Pre-equilibrium reaction**

It may just so happen that the emission of a particle is neither direct nor via a compound nucleus. At a time scale of  $\tau \sim 10^{-18}$  s, the projectile-target interaction reaches a state, where only a part of the target nucleus has acquired the energy from the projectile, and the state of statistical equilibrium, as in the case of a compound nucleus, has not yet been achieved. Nonetheless, the struck nucleons may abruptly initiate a cascade of interactions within the nucleus, upon which a nucleon may be emitted. Such reactions are called pre-equilibrium or pre-compound reactions and might be slightly forward peaked. [41, 42]

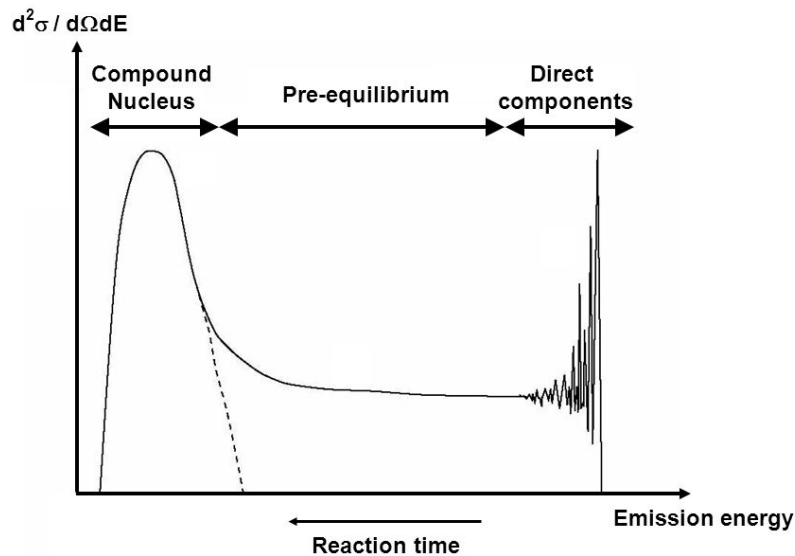


Figure 3.1: Plot of time and energy scale for different reaction mechanisms.

The mechanisms, however, display some mutual overlaps, as shown in Figure 3.1. At higher energies ( $> 50$  MeV), direct reactions become more probable and can be seen as sharpened peaks, and at energies below 15 MeV, the broad peaked compound formation is more likely to occur. The pre-equilibrium reactions dominate in between the two.

### 3.1.3 Proton Induced Nuclear Reactions

Table 3.1: Proton and deuteron induced reactions that yield monoenergetic neutrons. [33]

Incident particle	Reactions		
<i>proton</i>	${}^3\text{H}(p,n){}^3\text{He}$	${}^9\text{Be}(p,n){}^9\text{B}$	${}^{10}\text{B}(p,n){}^{10}\text{C}$
	${}^6\text{Li}(p,n){}^6\text{Be}$	${}^{10}\text{Be}(p,n){}^{10}\text{B}$	${}^{11}\text{B}(p,n){}^{11}\text{C}$
	${}^7\text{Li}(p,n){}^7\text{Be}$	${}^{12}\text{C}(p,n){}^{12}\text{N}$	${}^{15}\text{N}(p,n){}^{15}\text{O}$
	${}^{36}\text{Cl}(p,n){}^{36}\text{Ar}$	${}^{13}\text{C}(p,n){}^{13}\text{N}$	${}^{14}\text{C}(p,n){}^{14}\text{N}$
		${}^{39}\text{Ar}(p,n){}^{39}\text{K}$	${}^{59}\text{Co}(p,n){}^{59}\text{Ni}$
<i>deuteron</i>	${}^2\text{H}(d,n){}^3\text{He}$	${}^3\text{H}(d,n){}^4\text{He}$	${}^{24}\text{Mg}(d,n){}^{25}\text{Al}$
	${}^{13}\text{C}(d,n){}^{14}\text{N}$	${}^7\text{Li}(d,n){}^8\text{Be}$	${}^{18}\text{O}(d,n){}^{19}\text{F}$
	${}^{20}\text{Ne}(d,n){}^{21}\text{Na}$	${}^{15}\text{N}(d,n){}^{16}\text{O}$	${}^{32}\text{S}(d,n){}^{33}\text{Cl}$
			${}^{28}\text{Si}(d,n){}^{29}\text{P}$

Table 3.1 shows some of the reaction channels with various materials, wherein low-energy (p, n) and/or (d, n) reactions can lead to the production of monoenergetic neutrons. As mentioned earlier, at lower energies, the neutrons are produced mainly via de-excitation of an excited compound nucleus (see Figure 3.1 on the previous page). Thus, for the NOVA ERA facility (see Section 2.2.2 on page 14), where the proton energies range upto 10 MeV, the vital contribution to the neutron yield comes from compound reactions.

Figures 3.2 and 3.3 show the cross section of the main reaction channels triggered in Beryllium, with impinging protons and deuterons of varying energies. It is very clear from the figures that protons and deuterons at lower energies (< 20 MeV) have peculiarly high cross sections for (p, n) and (d, n) reactions, which peak at around 10 MeV. It is also directly observable that for energies around 10 MeV, the contributions from other reactions are significantly less. These findings are one of major reasons to operate the NOVA ERA facility with proton beam energy of  $\sim 10$  MeV (see Section 2.2.2 on page 14).

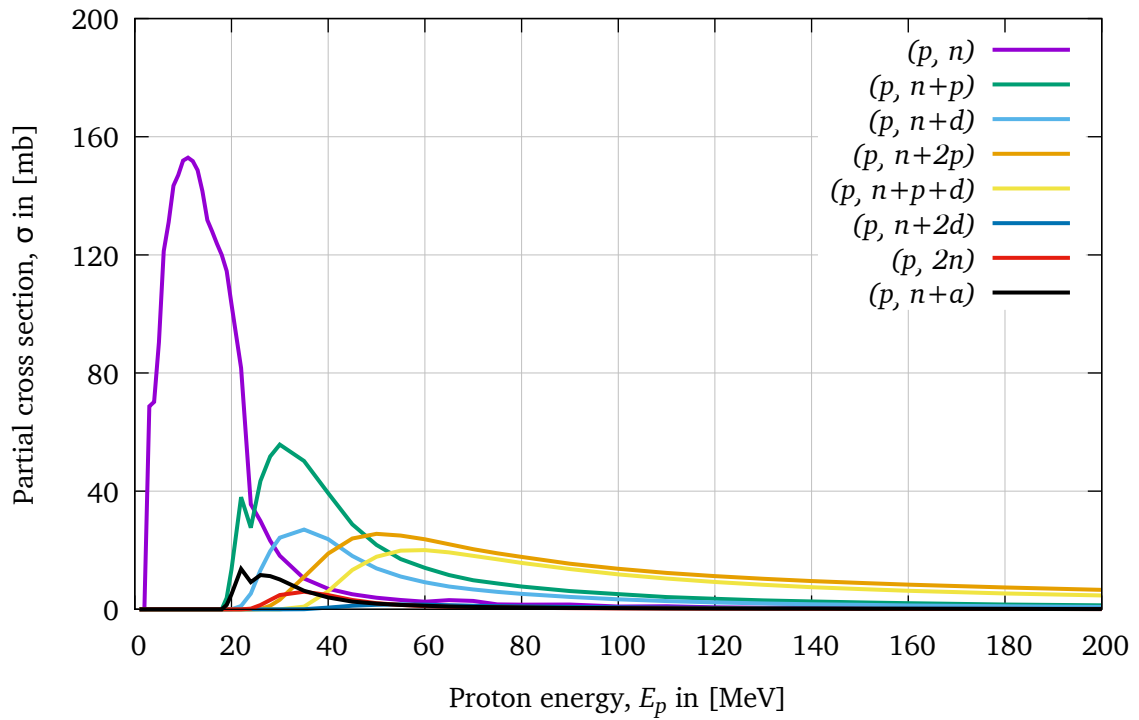


Figure 3.2: Partial cross sections of various reaction channels in Be with impinging protons. [45]

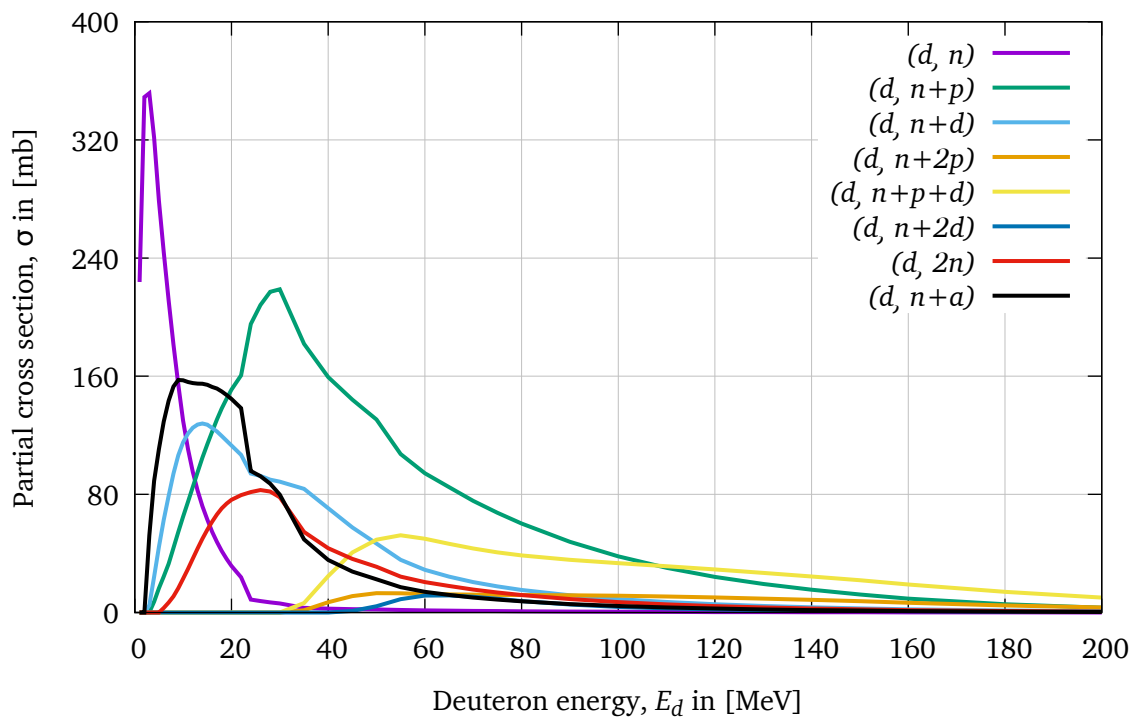


Figure 3.3: Partial cross sections of various reaction channels in Be with impinging deuterons. [46]

## 3.2 Electrons and their Interactions with Matter

Electrons are elementary charged particles that belong to the family of leptons<sup>2</sup> [47]. They interact with matter mostly via interactions with the atomic electrons and thus, lose energy in the process. However, due to their much lower mass ( $\sim 3$  orders of magnitude) compared to protons, they have comparatively a greater speed at any defined energy. As a consequence, their rate of energy loss per unit distance traversed in matter is much smaller [48, 49].

Their trajectories in matter are, nonetheless, much more complicated, since an electron loses a much greater fraction of its energy in a single interaction with another electron, owing to their comparable masses. Accordingly, their range in matter is much less well defined, and their linear distance of penetration will be very different from the length of the path they actually follow through the medium. Additionally, electrons also lose energy radiatively in form of ‘bremsstrahlung’, as their velocities change in any traversing medium (in the vicinity of nuclei) [48, 49].

For the purposes of this work, the maximum electron beam energy considered is 10 keV, and therefore any contribution due to radiative losses is significantly negligible. Hence, it is pragmatic to assume that all energy losses of such a low energetic electron beam in matter are strictly due to interactions with the bound atomic electrons, and that the complete energy is deposited in the material itself, in form of heat.

### 3.2.1 Electron-Beam Matter Interaction

As alluded in the previous section, electrons lose energy when traversing through matter. For an electron beam, this puts a limit on its penetration depth in any given medium. As electrons constantly lose their energy, due to such inelastic scatterings with the other bound atomic electrons, a mathematical description of this view is needed.

Since these interactions are inherently stochastic in nature, there is no absolute way of determining the exact penetration depth of a beam of a certain energy in

---

<sup>2</sup>Leptons, together with quarks, are the basic building blocks of all matter. However, contrary to quarks, leptons are not subject to the strong interactions.

a given medium. Moreover, there are also other interactions that come into play in reality. Even though the modified Bethe and Bloch equation [50] for scattering energy loss of electrons in matter gives a fine estimate of the distance that a beam of electrons can travel in a medium, this distance is measured along the complex trajectory that develops because of these other interactions [51].

To have a more meaningful estimate of the bulk of such interactions, the range of an electron beam can be described by the Kanaya–Okayama model [52]. This model is also employed in many Monte Carlo simulation codes to estimate the range of an electron beam (e.g. CASINO [53, 54], PENELOPE [55], etc.). The model encompasses the effects from both the elastic and inelastic interactions and gives an expression for the interaction volume in terms of the radius of a hemisphere centered on the beam impact point, which contains at least 95% of the total electron trajectories [51].

The equation reads as follows

$$R_{K-O} = 27.6 \cdot \left( \frac{A}{Z^{0.89} \cdot \rho} \right) \cdot E_0^{1.67}, \quad (3.1)$$

where

- $R_{K-O}$  is the expected Kanaya–Okayama range in [nm];
- $A$  is the atomic weight in [g/mol] of the given material;
- $Z$  is the atomic number of the given material;
- $\rho$  is the density in [g/cm<sup>3</sup>] of the given material; and
- $E_0$  is the incident beam energy in [keV].

This empirical formula is well validated and is used extensively in the field of electron microscopy [51]. Calculations of the Kanaya–Okayama range for materials of relevance to this work are presented in Table 3.2.

It is evident from these penetration depths that for such a low energetic electron beam, the heat deposition in the given materials can be approximated as a surface heat load (instead of a volume heat load, in case of 10 MeV protons). This also greatly simplifies the input heat parameters for the ANSYS CFX simulations (see Chapter 4 on page 40).

Table 3.2: Kanaya–Okayama range for given materials.

Material	Parameters				
	A	Z	$\rho$	$E_0$	$R_{K-O}$
	[g mol <sup>-1</sup> ]	[-]	[g cm <sup>-3</sup> ]	[keV]	[nm]
Steel	55.692	26	7.85	5.0	158
Al	26.981	13	2.70	5.0	413
Be	9.012	4	1.85	5.0	575

The average power of such a beam of electron with a defined energy and beam current is then given by the equation

$$P_{av} [\text{kW}] = E_{beam} [\text{MeV}] \cdot I_{beam} [\text{mA}] , \quad (3.2)$$

where

- $P_{av}$  is the average beam power;
- $E_{beam}$  is the beam energy; and
- $I_{beam}$  is the operational beam current.

Thus, a beam of 5 keV electrons operating at a peak current of 1 A exhibits or carries a transferable average beam power (or equivalently thermal power) of 5 kW.

### 3.3 Structural Mechanics

Structural mechanics is a branch of applied mechanics that deals with the computation and analysis of stresses, strains, and deformations in solid materials. This provides valuable insights into the strength, flexibility, and dynamic properties of a solid structure, thereby allowing the determination and safety assessment of the technical applicability of the given structure under static or transient loads of varying nature.

The study of structural mechanics is of great importance in the design, development, and safe operation of any mechanically constrained system. This is especially crucial in the context of material sciences, as it yields a better understanding of the mechanical behaviour of the materials being used. This also contributes to using appropriate mathematical models required to describe the physical system. In most cases, fitting numerical and simulation techniques are employed to investigate the system's response to applied loads.

In real-life problems, most systems are *statically indeterminate*, meaning that the forces in the system cannot be computed merely by considering the equilibrium conditions. This requires the inclusion of deformations, in order to determine the forces in the system. Thus, the static indeterminacy causes the structural analysis to be expressed in terms of three types of equations, each describing a particular relation within the system. These are:

- **Stress and equilibrium equations**

These are the set of equations resulting from the Newton's second law of motion. In terms of internal stresses in solid bodies, these can be expressed as

$$\nabla \cdot \sigma + \mathbf{f} = \rho \cdot \frac{\partial^2 \mathbf{u}}{\partial t^2}, \quad (3.3)$$

where  $\sigma$  is the stress tensor,  $\mathbf{f}$  is the force per unit volume,  $\rho$  is the mass density, and  $\mathbf{u}$  is the displacement vector.

- **Strain and compatibility equations**

These are the set of geometric equations that describe the relation between the engineering strains and the displacement field in a solid. Mathematically these are expressed as

$$\nabla \times (\nabla \times \epsilon) = \mathbf{0}, \quad (3.4)$$

where  $\epsilon$  is the strain tensor.

- **Constitutive empirical relations**

These form the set of material equations that relate stresses to strains. For linear elastic materials, i.e. materials in which the stresses vary linearly with strains, constitutive relations are often unique. However, as the materials

deviate from this behaviour, these relations become more and more empirical and must be found out via measurements. For linear elastic materials, these equations are described by the Hooke's law as

$$\sigma = \mathbf{C} \cdot \epsilon, \quad (3.5)$$

where  $\mathbf{C}$  is the symmetric  $6 \times 6$  stiffness or elasticity tensor, and  $\sigma$  and  $\epsilon$  are expressed as  $6 \times 1$  column vectors of stress and strain components, respectively. The components of the stiffness tensor are expressed in terms of the Young's modulus of elasticity,  $E$ , and the Poisson's ratio,  $\nu$

$$\mathbf{C} = \frac{E}{(1 + \nu) \cdot (1 - 2 \cdot \nu)} \cdot \begin{pmatrix} (1 - \nu) & \nu & \nu & 0 & 0 & 0 \\ \nu & (1 - \nu) & \nu & 0 & 0 & 0 \\ \nu & \nu & (1 - \nu) & 0 & 0 & 0 \\ 0 & 0 & 0 & \frac{(1-2 \cdot \nu)}{2} & 0 & 0 \\ 0 & 0 & 0 & 0 & \frac{(1-2 \cdot \nu)}{2} & 0 \\ 0 & 0 & 0 & 0 & 0 & \frac{(1-2 \cdot \nu)}{2} \end{pmatrix} \quad (3.6)$$

Thus, Equations 3.3-3.5 together yield a set of 15 algebraic equations that are linearly independent and must be solved to obtain stresses and deformations in a solid body bearing loads, but only for linear elastic materials. For other materials, such as metals at elevated temperatures, plastics, rubber, etc. further equations and empirical relations are needed to completely describe the system.

For cases, where the system is under additional thermal loads, such as a linear isotropic metal, the thermal strain thus produced depends on a material specific constant,  $\alpha$ , known as the coefficient of thermal expansion. This new strain depends on the temperature difference caused by the thermal load,  $\Delta T$ . Equation 3.5 then transforms to:

$$\sigma = \mathbf{C} \cdot \epsilon + \epsilon^{\mathbf{T}}, \quad (3.7)$$

where

$$\epsilon^T = \begin{pmatrix} \frac{E \cdot \alpha \cdot \Delta T}{(1 - 2 \cdot \nu)} \\ \frac{E \cdot \alpha \cdot \Delta T}{(1 - 2 \cdot \nu)} \\ \frac{E \cdot \alpha \cdot \Delta T}{(1 - 2 \cdot \nu)} \\ 0 \\ 0 \\ 0 \end{pmatrix} \quad (3.8)$$

Therefore, the stress can be expressed as a linear function of the temperature difference in a rigid body.

### 3.3.1 Failure Mechanisms

In practical cases, it is necessary that the integrity of a solid structure is not compromised and that it can withstand the given loads under all circumstances. This is the main aim of performing a structural mechanics analysis. It is done to validate solid structures for given load situations. In order to do so, failure criteria are introduced that conservatively reduce the allowed loads by a safety factor to take into consideration various aspects, such as uncertainties in material data, manufacturing tolerances, and assumptions made in analysis.

For solid structures and static conditions, the decisive factor is the overall stress that builds up within the solid. At no point should these stresses exceed the ultimate yield strength of the material, which is when it breaks. As a result, the safety factor is expressed as a ratio of the material's yield strength to the maximum possible applied stress, and is usually between 1.5 to 3, depending on the regulations that are needed to be applied.

### 3.3.2 Finite Element Method (FEM)

However, significant evidence currently stands against the practice of applying traditional deterministic methods to properly design and characterize complex structures and their components, when subjected to a range of intricate loading

conditions. Based on inherently complicated geometrical configuration, nonlinear material behaviour, and various other uncertain aspects, more advanced computational tools, such as finite element methods (FEMs), finite difference methods (FDMs), or boundary integral equation methods (BIEMs), must be adopted in successfully analyzing the target components of a CANS. Since ANSYS simulations presented in this research work are all built on FEM, it suffices to follow only the relevant FEM theory (see Chapter 4 on page 40). [56]

### 3.4 Thermal Radiation

Measurement (and simultaneous acquisition) of surface temperatures of a given body via a non-invasive, accurate, and fast technique is a well sought-after approach in many fields of research and especially in industrial processes, such as material welding, waste incineration, hotspot detection in solar panels, etc.

Amongst many that currently exist, a fast and efficient remote temperature sensing technique has been employed in this work to provide a measure of the surface temperatures achieved by the investigated target materials (see Section 5.2 on page 55), namely *radiation pyrometry*<sup>3</sup>. This approach exploits the fact that all bodies give off thermal radiation above absolute zero (0 K).

Thermal radiation is electromagnetic radiation that is emitted by matter due to the changes in its thermal state (variation of its internal energy), whose wavelength typically lies in the range of 0.1  $\mu\text{m}$  to 100  $\mu\text{m}$ , as shown in Figure 3.4 on the next page. Consequently, it includes a part of the ultraviolet (UV), and all of the visible and infrared (IR) radiation. [57–60]

The spectrum of this emitted radiation (i.e., the intensity vs. wavelength curve) from a body is a function of its temperature, emissivity (see Sec. 3.4.1.2 on page 36), and other surface properties, and it often follows the idealized black-body radiation curve (see Figure 3.5 on page 35). Additionally, the distribution of the emitted radiation is highly directional in most cases, i.e., the surface contributing to the

---

<sup>3</sup>Radiation pyrometry is the area of surface temperature measurement, wherein the emitted thermal radiation of a body is used to determine the temperature of that body.

emission particularly favours a certain direction, usually due to its shape and geometrical orientation. [57–60]

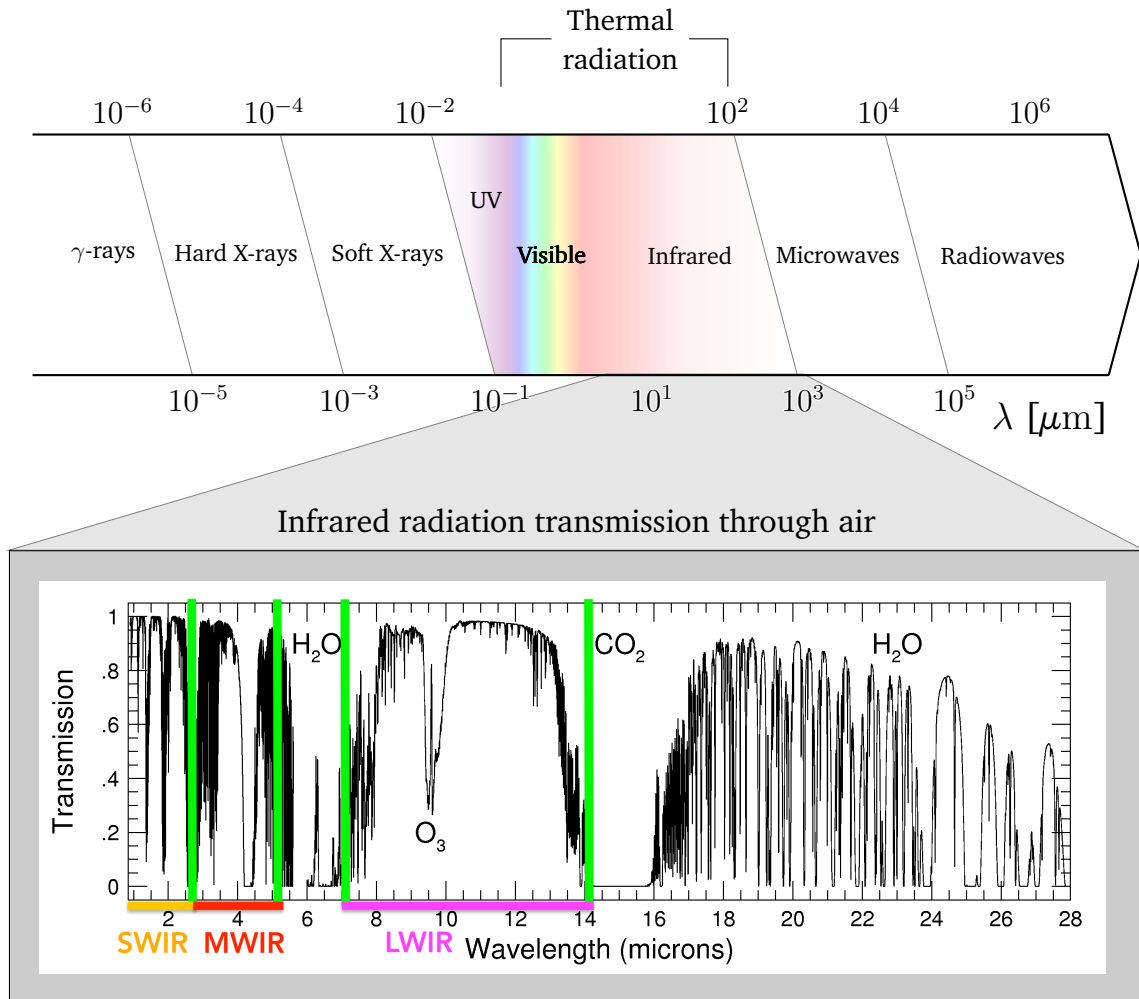


Figure 3.4: The range of thermal radiation in the electromagnetic spectrum, along with the IR transmittance in air between 1  $\mu\text{m}$  and 28  $\mu\text{m}$ . The transmission vs. wavelength plot has been taken from [61].

### 3.4.1 Black Body and Blackbody Radiation

The interaction of incident electromagnetic radiation onto a body (in the context of radiometry<sup>4</sup>) can only happen in the following three ways:

- i partial or complete reflection from its surface;

<sup>4</sup>Radiometry is the branch of science that deals with the measurement of electromagnetic radiation, particularly in the ultraviolet, visible, and infrared ranges.

- ii partial or complete absorption by it; and
- iii partial or complete transmission through it.

Quantitatively, the individual probabilities of these processes to occur are described by three different dimensionless coefficients, namely the reflectance  $\rho(\lambda)$ , the absorptance  $\alpha(\lambda)$ , and the transmittance  $\tau(\lambda)$ . As is clear from the expressions, the coefficients are all dependent on the wavelength of the incident radiation. Besides wavelength, the directional distribution of the irradiation can also be an influential factor in some cases. [60]

It, thus, follows directly that the sum of these three coefficients must be unity, in accordance with the law of conservation of energy

$$\rho(\lambda) + \alpha(\lambda) + \tau(\lambda) = 1. \quad (3.9)$$

A body that can potentially absorb all the irradiating electromagnetic radiation, irrespective of its wavelength and directionality, is defined as an ideal black body. Hence, by definition, it is also implied that a black body is a perfect emitter of radiation at every wavelength and in every direction, lacking which the first law of thermodynamics would not hold true. Appropriately so, the emitted thermal radiation from a black body is called the blackbody radiation. As a result, for an idealized black body,  $\alpha(\lambda) = 1$  and  $\rho(\lambda) = \tau(\lambda) = 0$ . [57–60]

#### 3.4.1.1 Planck's Law

In order to mathematically characterize the emitted thermal radiation by a body, Max Planck, in the early 1900's, empirically derived a relation between the emitted spectral radiation density by a black body that is in a state of thermal equilibrium with its surroundings and its temperature. This relation is the famous Planck's law. The energy density per unit frequency interval (or per unit wavelength interval) for a blackbody radiation is then given by the Planck's formula as follows

$$u_\nu(\nu, T) \cdot d\nu = \frac{8 \cdot \pi \cdot h \cdot \nu^3}{c^3} \cdot \frac{1}{e^{(h\nu/kT)} - 1} \cdot d\nu; \quad (3.10)$$

$$u_{\lambda}(\lambda, T) \cdot d\lambda = \frac{8 \cdot \pi \cdot h \cdot c}{\lambda^5} \cdot \frac{1}{e^{(h \cdot c / \lambda \cdot k \cdot T)} - 1} \cdot d\lambda, \quad (3.11)$$

where

- $u_{\nu}(\nu, T)$  is the energy density per unit frequency interval,
- $u_{\lambda}(\lambda, T)$  is the energy density per unit wavelength interval,
- $d\nu$  is an infinitesimally small frequency interval,
- $d\lambda$  is an infinitesimally small wavelength interval,
- $h$  is the Planck's constant,
- $\nu$  is the frequency,
- $\lambda$  is the wavelength,
- $c$  is the speed of light in vacuum,
- $k$  is the Boltzmann constant, and
- $T$  is the absolute temperature. [57, 62, 63]

However, for most practical applications, oftentimes the radiometric quantity *spectral radiance*<sup>5</sup>, based on Equations 3.10 and 3.11, is used, which can be expressed mathematically as

$$L_{BB,e,\lambda,\Omega}(\lambda, T) = \frac{2 \cdot h \cdot c^2}{\lambda^5} \cdot \frac{1}{e^{(h \cdot c / \lambda \cdot k \cdot T)} - 1}, \quad (3.12)$$

where the subscripted  $BB$  and  $e$  stand for 'blackbody' and 'energetic', respectively, and are used as conventions to denote radiometric quantities. However,  $\lambda$  and  $\Omega$  show the 'wavelength' and the 'solid angle' dependence, respectively. [62, 63]

Figure 3.5 on the following page depicts the spectral radiation curve of an ideal back body at different temperatures, with almost entirely radiating in the IR region (shaded part). It is also noticeable that for higher temperatures, the curve becomes narrower and peaks towards the lower wavelength region. Furthermore, the area under the spectral radiance curve relates the absolute temperature of the body to its radiated power according to the Stefan-Boltzmann law, which states that the total emitted radiation of a black body is equal to the fourth power of its absolute

<sup>5</sup>Spectral radiance is the radiant flux or power emitted by a surface per unit solid angle per unit projected area per unit frequency or wavelength. It is very commonly expressed in the units of [ $\text{W sr}^{-1} \text{m}^{-2} \text{nm}^{-1}$ ] and is represented by the symbol  $L$ .

temperature, i.e.,

$$L_{BB,\Omega} = \int_0^{\infty} L_{BB,e,\lambda,\Omega}(\lambda, T) \cdot d\lambda \cdot dT = \sigma \cdot T^4, \quad (3.13)$$

where

$L_{BB,\Omega}$  is the radiant intensity, i.e., the directional radiant power, and  
 $\sigma$  is the Stefan-Boltzmann constant. [62, 63]

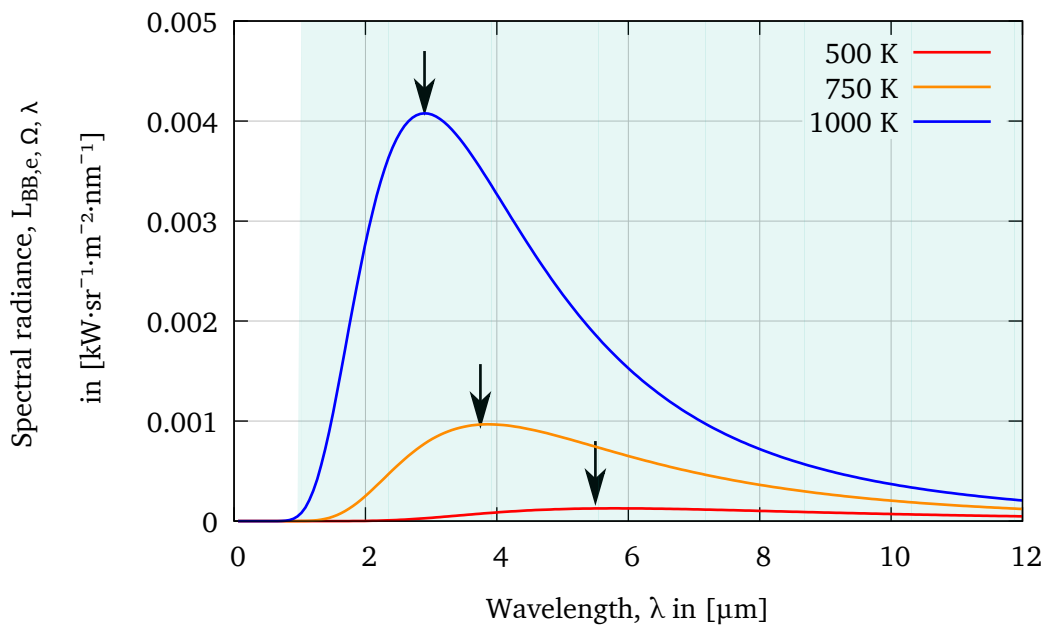


Figure 3.5: Spectral radiance of an ideal black body at different temperatures, as calculated from Equation 3.12. The arrows point to the peak-maximum.

The notion of a black body plays a key role in studying thermal radiation and electromagnetic radiation energy transfer. In practice, there exists no ideal black body, and so the absorbing and emitting capacities of real bodies are always below 1. It, thus, becomes necessary to understand, how and to what extent the absorbing and emitting capacities of real bodies deviate from that of an ideal black body's. [57]

### 3.4.1.2 Emissivity and Kirchoff's Law

As mentioned above, real bodies do not exhibit the perfect black body behaviour. For real bodies, the thermal emission depends greatly on their optical properties. Therefore, how strongly or weakly a real body correlates to a black body is defined by the ratios of their respective spectral radiances at any given temperature. This ratio is called the emissivity  $\varepsilon(\lambda)$  of the given body. Emissivity of a body also depends on the body's temperature and surface properties and is, like absorptance, also a dimensionless quantity. For a perfect black body  $\varepsilon(\lambda)$  is, therefore, unity. By definition

$$\varepsilon(\lambda) = \frac{L_{e,\lambda,\Omega}}{L_{BB,e,\lambda,\Omega}}. \quad (3.14)$$

If a body at some temperature above absolute zero, in a closed system, is also in thermal equilibrium with its surroundings, it follows directly that it must simultaneously also absorb radiation energy, in order to maintain this state of equilibrium. As a result, at any given wavelength, the body must absorb and emit the same amounts of radiation, failing which the system would lose the equilibrium. This phenomenon is known as Kirchoff's law of thermal radiation. This means that for any body in thermal equilibrium

$$\alpha(\lambda) = \varepsilon(\lambda) \quad (= 1 \text{ for an ideal black body}). \quad (3.15)$$

For real bodies however, the emissivity is only a fraction between 0 and 1, as is absorptance. There is an exception to this statement, since there exist objects that may exhibit, under certain conditions, emissivities greater than 1 [60]. This is, nonetheless, out of the scope of this work and shall not be discussed. For the purposes of this work, it suffices to adhere only to bodies with  $0 < \varepsilon(\lambda) < 1$ .

Emissivity, thus, allows for the measurement of surface temperatures of real bodies by correlating their emitted spectral radiances to ideal black bodies', i.e.,

$$L_{e,\lambda,\Omega} = \varepsilon(\lambda) \cdot L_{BB,e,\lambda,\Omega}. \quad (3.16)$$

From Equation 3.13, it also follows that the radiated power by a real body is:

$$L_{\Omega} = \varepsilon(\lambda) \cdot \sigma \cdot T^4. \quad (3.17)$$

Equations 3.16 and 3.17 form the basis of the modern day radiation pyrometry and thermography<sup>6</sup>.

For most pure metals and oxides with smooth surface, the emissivity is generally low, independent of the wavelength, and increases with the temperature, as shown in Equation 3.18 [64].

$$\varepsilon_T = 0.5736 \cdot \sqrt{\rho(T) \cdot T} - 0.1769 \cdot \rho(T) \cdot T, \quad (3.18)$$

where  $\rho(T)$  is the temperature dependent volume resistivity of the material. A linear approximation for the resistivity of pure metals can be used, if the temperature range does not vary drastically, as given in Equation 3.19.

$$\rho(T) = \rho_0 \cdot [1 + \alpha \cdot (T - T_0)], \quad (3.19)$$

where

$\varepsilon_T$	wavelength independent emissivity,
$T$	is the absolute temperature,
$T_0$	is the absolute reference temperature, and
$\alpha$	is the temperature coefficient of resistivity.

### 3.4.2 Temperature Estimation

As mentioned above, the temperature of a body can be determined from its emitted thermal radiation, given that the emissivity is known. Since, most measuring sensors or devices are only sensitive in defined bands of the electromagnetic spectrum, the emissivity in the specific detection range must be either measured or known

<sup>6</sup>Thermography is the technique of investigating and measuring temperatures of bodies via thermal imaging, mostly in the (near and far) IR regions.

beforehand. For almost all practical applications and purposes, this detection window lies in the IR region. This is because, bodies that are not too hot (several hundred degrees Celsius) emit mostly in the IR region, as is shown in Figure 3.5 on page 35. This also allows for the measurement of temperatures that are even below the room temperature. [60]

From Equation 3.15, only bodies that have high absorptance, will have a high emissivity. Thus, the true surface temperature of a body can be only concluded, if the emissivity of the body is close to 1 and does not vary locally with the body's surface area. Under these conditions, the influence of transmittance and reflectance by the object can be neglected, and the temperature values can be determined. [60]

An important aspect to be considered is the employed detection range. Usually measurements take place in places, where air is the propagating medium for the thermal radiation, before it reaches the detection devices. The composition of air renders the transmission of certain wavelength impossible, for the photons corresponding to these wavelengths are greatly absorbed or scattered by the air molecules, as shown in Figure 3.4 on page 32. Thus, the detection wavelength range must be so chosen such that these dominant absorption regions are avoided. [60]

As illustrated in Figure 3.4 on page 32, in the relevant IR range of  $1 \mu\text{m}$  to  $30 \mu\text{m}$ , there are typically 3 windows, where the absorption of thermal radiation in the air is, for all practical purposes, negligible. These are the so called:

- i SWIR - short-wavelength IR ( $\sim 1\text{-}2.5 \mu\text{m}$ );
- ii MWIR - mid-wavelength IR ( $\sim 2.7\text{-}5 \mu\text{m}$ ); and
- iii LWIR - long-wavelength IR ( $\sim 7\text{-}14 \mu\text{m}$ ). [60]

### 3.4.3 Radiation Pyrometer Devices

A radiation pyrometer is a non-contact, non-intrusive thermometer that evaluates the temperature of a given surface by means of its emitted thermal radiation. These typically measure the spectral radiance at specific wavelengths. The number of available spectral lines from such a radiance spectrum depends on the temperature of the measured body. At temperatures relevant for this work and due to the employed pyrometer, the MWIR band is where the radiance is measured (see

Section 5.2 on page 55).

The measured radiance of the spectral lines also depend on various optical elements that lie between the pyrometer sensor and the scoped surface. Assuming a linear temperature dependence of all the contributing optical elements (such as the optical mirror and the sapphire glass; see Figure 5.4), a parameter,  $o(\lambda, T)$ , can be associated with Equation 3.17 to fully characterize the measured spectral radiance by the pyrometer such that

$$L'_{\Omega} = o(\lambda, T) \cdot \varepsilon(\lambda) \cdot \sigma \cdot T^4 \quad (3.20)$$

or

$$L'_{\Omega} = \varepsilon(\lambda)' \cdot \sigma \cdot T^4, \quad (3.21)$$

where

$o(\lambda, T)$       optical parameter, and  
 $\varepsilon(\lambda)'$       modified emissivity.

## Chapter 4

---

# Simulation

---

While the practicality and relative simplicity of handling a thermionic electron gun (referred hereafter as e-gun), capable of producing energetic beams of upto 10 keV, is a good starting source, it is very difficult to analytically predict the outcome of an arbitrary beam power being introduced on to the target surface. The target disc must be able to withhold and sustain the power deposition under operation, especially at higher loads. Thus, a prior assessment of the structural integrity of the target disc under varying (thermal and mechanical) loads must be conducted to ensure a safe and sensible experimental setup.

There is yet another challenge posed by the e-gun, before any experimental tests can be done with it. The beam profile of a tungsten filament that produces the electrons depends greatly on the shape of the filament. Thus, a helical spring-shaped filament (as is the case with the e-gun employed for this work) is not expected to produce a gaussian beam profile, which is the requirement on the NOVA ERA accelerator. This must, therefore, be corrected for and characterized before setting up the test station.

Consequently, thermo-mechanical simulation studies for the same must be carried out beforehand, in order to better understand, characterize, and analyze the problems associated with the thermal and structural deformations within the target due to the impinging electrons. A series of such simulation work will not only be helpful in determining the underlying engineering challenges that delimit the target configurations for the NOVA ERA facility but also in successfully planning and executing the experiments at a later stage.

This chapter provides a concise yet thorough overview of the geometry, simulation parameters, and natural and essential boundary conditions for the mathematical modelling that embodies the simulation setup. As mentioned in Section 2.3.2 on page 16, the simulations are performed only in consideration of the NOVA ERA target geometry.

## 4.1 Beam Modelling

For the purposes of this work, the electron beam is assumed to have a 2D circular symmetric gaussian profile. This is then used to determine the average heat flux deposited in the target. The stepwise 2D gaussian heat flux profile based on this assumption significantly helps to simplify the simulations in ANSYS.

A general normalized 2D Gaussian distribution function,  $G^2(x, y)$ , is defined as follows

$$G^2(x, y) = \frac{1}{\sqrt{2 \cdot \pi} \cdot \sigma_x} \cdot \frac{1}{\sqrt{2 \cdot \pi} \cdot \sigma_y} \cdot e^{-\left(\frac{(x - \mu_x)^2}{2 \cdot \sigma_x^2} + \frac{(y - \mu_y)^2}{2 \cdot \sigma_y^2}\right)}, \quad (4.1)$$

where

- $\sigma_x$  is the standard deviation in  $x$ ;
- $\sigma_y$  is the standard deviation in  $y$ ;
- $\mu_x$  is the expectation of  $x$ ; and
- $\mu_y$  is the expectation of  $y$ .

For a symmetric Gaussian distribution centered at the origin  $O(0, 0)$ ,  $G^2(x, y)$  reduces to the form

$$G^2(x, y) = \frac{1}{2 \cdot \pi \cdot \sigma^2} \cdot e^{-\left(\frac{x^2 + y^2}{2 \cdot \sigma^2}\right)}, \quad (4.2)$$

where

- $\sigma_x = \sigma_y = \sigma$ ; and
- $\mu_x = \mu_y = 0$ .

The probability density function,  $P(\{x, y\} | \sigma^2)$ , of this Gaussian distribution within a given closed interval can then be determined mathematically via double integration (see Appendix 6). The expectation values within appropriately predefined  $\sigma$  ranges (see Table A2.4) are then associated with the heat flux values to build the aforementioned stepwise 2D gaussian heat flux profile. This results in the division of the beam spot (30 mm) in a given number of concentric circular regions, each encompassing an average heat flux value corresponding to the gaussian distribution, as shown in Figure 4.1. The number of circular regions in turn vary in accordance with the beam profile.

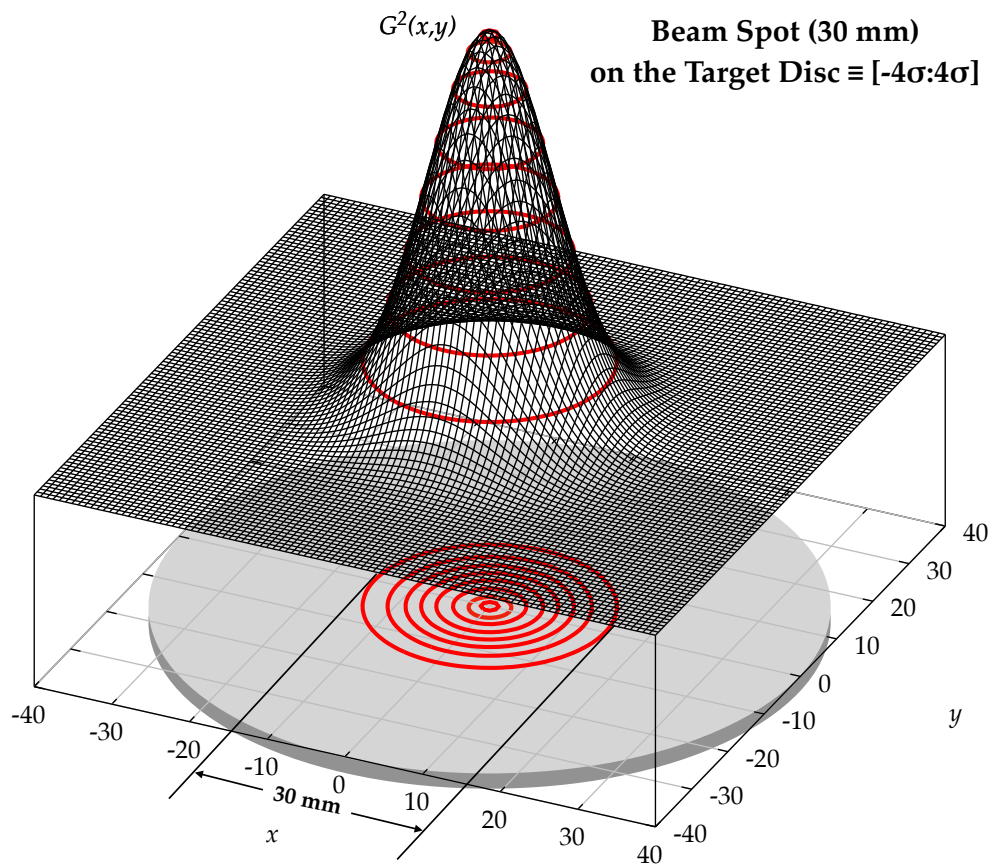


Figure 4.1: The gaussian heat flux distribution on the target surface for a narrow beam focused entirely on the beam spot.

## 4.2 Simulation Parameters

In order to gain faster computational times, the geometry was also reduced to a 1/22nd slice of the whole target geometry due to its rotational symmetry. This part

was then discretized into finite elements using the inbuilt ANSYS Mesh Modeler, as shown in Figure 4.2. Moreover, a mesh analysis has been performed in order to outweigh any mesh induced dependencies on the results of the simulations. For better convergence, a conformal mesh setup is used in order to avoid (additional) interpolations necessary at interfaces between different components of the target assembly.

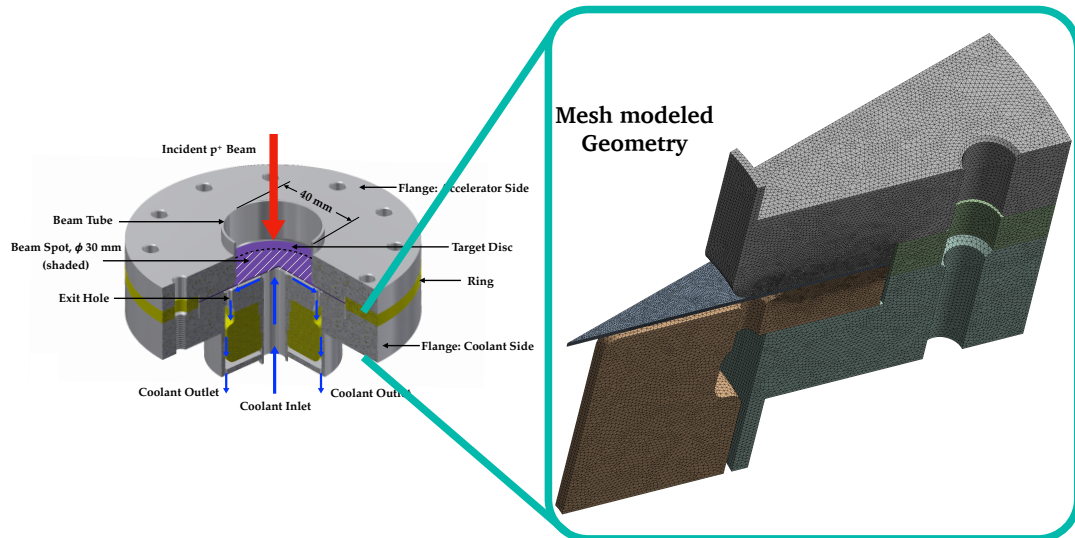


Figure 4.2: Reduced ANSYS model of the target geometry with meshing.

The geometry, nonetheless, is still only a good virtual representation of the actual design. Numerous constraints have to be assigned to the design, before it can describe the real physical problem to be solved numerically using ANSYS. Thus, several parameters are specified to approach the real physical conditions, as shown in Figure 4.3. Together with the defined contact regions between various components of the target assembly, a comprehensive mathematical model is delineated to ANSYS, which is then numerically solved within the bounds of the predefined convergence criteria. The energy, mass, and momentum equations for the CFD are solved for each finite volume with the shear-stress transport model (SST) [65].

Since the complete energy transfer from the electron beam is assumed to be deposited within the target in form of surface heat, this heat flux is mathematically modeled as a stepwise 2D gaussian heat flux profile (varying with power and standard deviation) in ANSYS CFX (see Section [ref.]). The simulation matrix consists of 3x5 cases for each material, with varying beam power (0.1 kW, 0.4 kW, 1.0 kW, 2.5 kW, and 5.0 kW) and varying beam's standard deviation—corresponding

to the beam spot radius of 15 mm on the target ( $2\sigma$ ,  $3\sigma$ , and  $4\sigma$ ). All the specified parameters for the simulations are listed below:

**E: Static Structural**

Static Structural

Time: 1. s

2/27/2019 2:04 PM

- A** Imported Pressure
- B** Vacuum:  $-1.e-011$  MPa
- C** Fixed Support
- D** Fixed Support 2
- E** Fixed Support 3
- F** Fixed Support 4
- G** Fixed Support 5
- H** Fixed Support 6
- I** Force: 1112.1 N
- J** Force 2: 1112.1 N

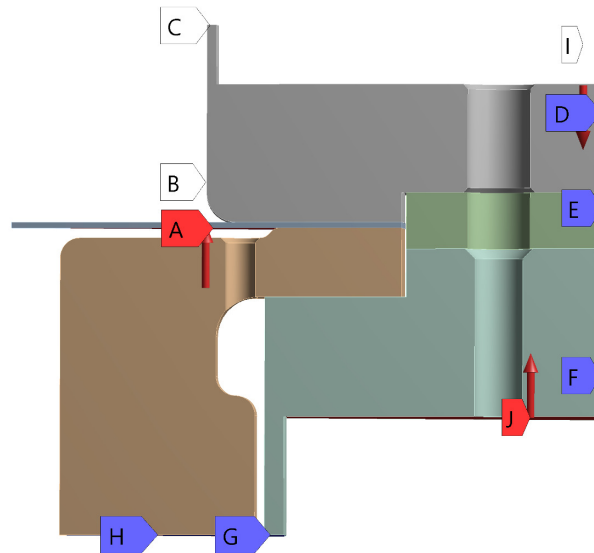


Figure 4.3: The assigned physical constraints to the designed model, in order to numerically evaluate the thermal and mechanical stresses in the target.

- *ANSYS CFX*

Coolant water velocity normal to the bottom surface of the target disc:

3 m/s.

Vacuum pressure on the top of the target disc:  $10^{-7}$  mbar.

Coolant water exit average pressure: 0.1 bar.

Coolant water inlet temperature:  $20^{\circ}\text{C}$ .

Material parameters such as thermal conductivity, thermal expansion coefficients, density, etc. were imported from the ITER material database [66].

- *ANSYS Mechanical*

The loads and supports are defined as shown in Figure 4.3. *I* and *J* are the compression forces, calculated analytically, resulting from a screwed joint.

The temperature and pressure values are imported from ANSYS CFX.

### 4.3 Results and Discussions

As mentioned in the previous section, the beam profile is varied as a function of its standard deviation, which corresponds to the beam spot diameter. Three beam profiles were considered for the simulations:

- $4\sigma$  - beam, where  $[-4\sigma:4\sigma]$  corresponds to 30 mm;
- $3\sigma$  - beam, where  $[-3\sigma:3\sigma]$  corresponds to 30 mm; and
- $2\sigma$  - beam, where  $[-2\sigma:2\sigma]$  corresponds to 30 mm.

#### 4.3.1 Thermal Results

Table 4.1: Maximum permissible thermal load for proposed target materials.

Material	Maximum power that can be deposited for		
	$4\sigma$ - Beam	$3\sigma$ - Beam	$2\sigma$ - Beam
	[kW]	[kW]	[kW]
Steel	2.45	4.00	> 6
Aluminium	1.90	3.00	4.15
Beryllium	1.75	2.75	4.80

The main thermal results are shown in Figure 4.1 (A) and Figure 4.2 (A). The temperature values are plotted for the nominal beam power, i.e. the fraction of beam power lying within the beam spot (almost 100% for a  $4\sigma$  - beam, 98.89% for a  $3\sigma$  - beam, and 86.47% for a  $2\sigma$  - beam). As expected, the maximum temperature in the target increases with the beam power and decreases with beam divergence, i.e. as the beam diameter spreads out and is less localized at the beam spot. The temperatures rise as high as 4237 K for Beryllium, 1935 K for Aluminium, and 3018 K for Steel for a well-focused  $4\sigma$  - Beam. This already exceeds the melting points of the respective materials, sketched in yellow in Figure 4.1 (A). The plots, thus, reveal the maximum power that can be deposited in the target materials for various

beam profiles, as shown in Table 4.1. As a consequence, employing a narrow  $4\sigma$  - beam at higher beam powers is clearly a poorly chosen arrangement for a real scenario.

### 4.3.2 Structural Results

The maximum equivalent Von Mises stresses in the target are shown in Figure 4.1 (B) and Figure 4.2 (B). The stresses build up as a combined result of (i) the coolant water pressure from below the target, (ii) the high vacuum conditions on the top of the target, (iii) the thermal loads due to the electron beam, and (iv) the physical structural constraints to hold the target in position. The integrated stress values are also plotted for the nominal beam power, as mentioned in the previous case. Here also, the maximum stress values increase with the beam power and decrease with the beam divergence. To maintain the structural integrity, the maximum reachable stress values must not increase the yield strength of the respective materials. This imposes an additional restriction to the extent of beam power that can be employed, in order to safeguard the structural failures in the target. From Appendix 6, it is obvious that exceeding the beam power beyond 1 kW overshoots the yield strengths for all materials.

In order to remain well below the yield strengths of the materials, a  $2\sigma$  - beam operated at power levels below 1 kW can be used. This not only ensures lower temperature values in the target but simultaneously decreases the stress induced deformations, as shown in Figure 4.1 (C) and Figure 4.2 (C).

At this point, it is also noteworthy to mention that although an even broader beam profile may further reduce the stresses and temperatures in the target, thus allowing for higher beam powers, it loses most of its intensity in regions lying outside the beam spot. Thus, a gaussian beam, whose  $-1\sigma:1\sigma$  range lies within the beam spot, loses almost 60% of its beam power to areas lying outside the beam spot, extending over to the target housing. This results in more than half of the beam getting wasted, which is rationally an impractical approach. Therefore, beams, broader than those simulated, are not accounted for in this work.

A detailed summary of the results from all the simulations is also tabulated in Table 4.2. It is, thus, also clear that an optimum out of the highest employable beam power, the least loss incurred in fraction of beam incident on the target, and

the resulting structural and thermal conditions in the target is reflected when using the wide  $2\sigma$  - beam profile. The ANSYS simulation results for a  $2\sigma$  - beam at 0.1 kW are also illustrated pictorially in Figure 4.3.

The thermal and structural results for different materials for the above case are also presented separately in Figure 4.4. The comparison shows that while thermally the materials do not behave very differently, Aluminium clearly stands out as the most stable material structurally followed by Steel and Beryllium, respectively. While this distinctly makes Aluminium the material of choice, a major decisive factor for the material would be the neutron yield at the end, which is out of the scope of this work and so is not considered.

### 4.3.3 Discussions

The model used to analyze the effect of the induced heat from an electron beam to the target materials is an idealized model. Firstly, all the components of the target assembly are assumed to be in perfect thermal contact and, secondly, any frictional motion between the components was not taken into consideration. The heat flux is also not described as a perfectly smooth gaussian distribution (only as a stepwise profile), and therefore, it will also have an influence on the absolute temperature values, and consequently on the stresses generated by ANSYS. Also, as the beam gets broader or more divergent, there is a tail of the gaussian distribution that is not confined within the target and spreads over to the target housing. This fraction of the beam power is then neglected, since it does not contribute to the heating effects in the target. However, there may be some indirect structural influences on the target due to the resulting heated up housing, which are then also not taken into consideration.

Whole Power Range: 0 kW - 5 kW

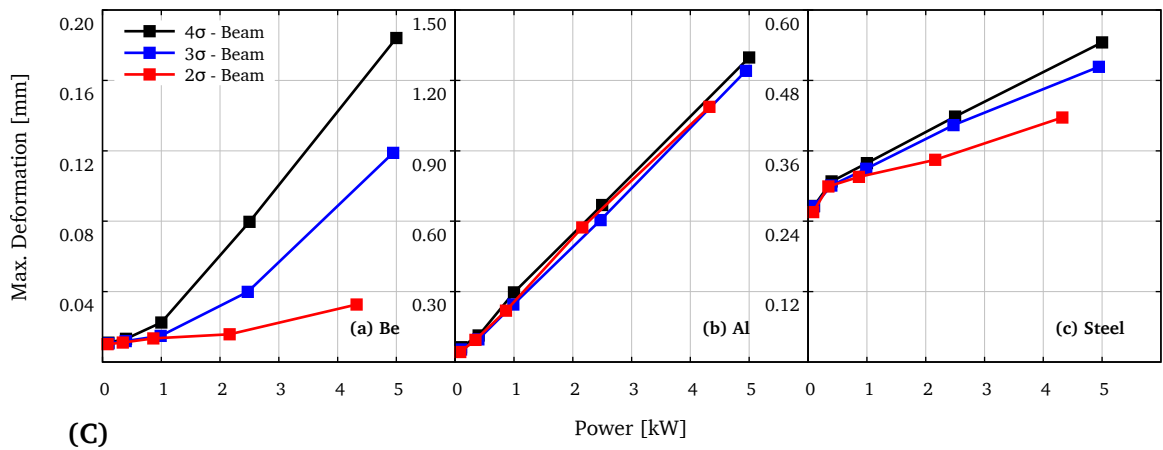
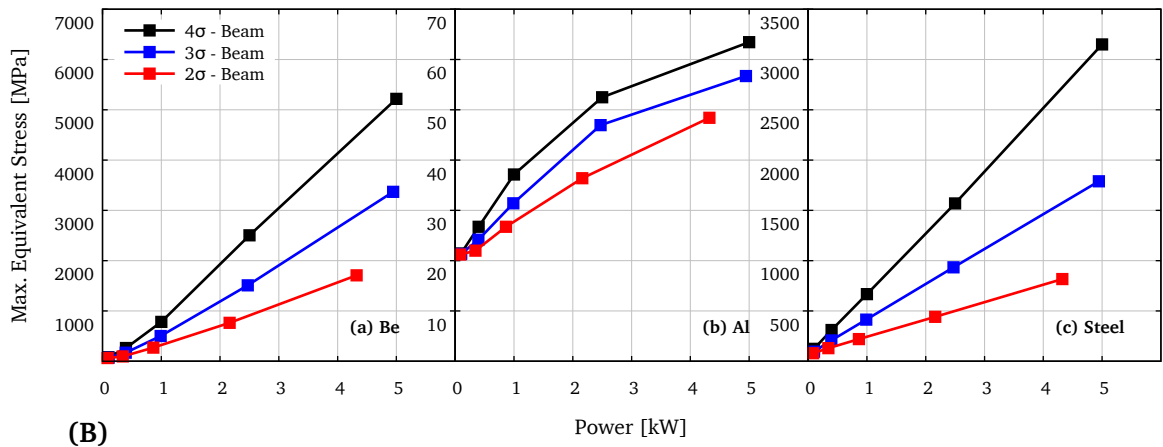
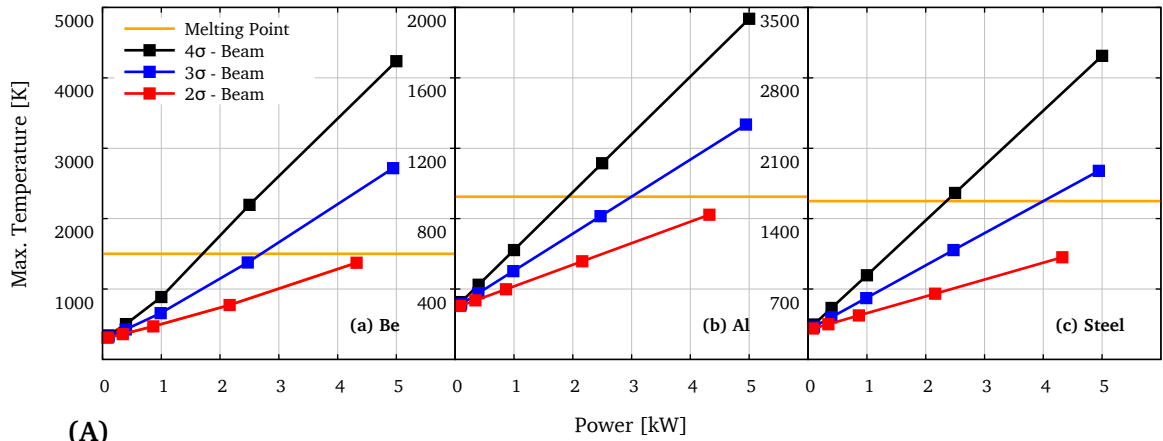


Figure 4.1: Maximum temperature, stress, and deformation values reached within the target materials, for varying beam power and beam profiles.

Power Range: 0 kW - 1 kW

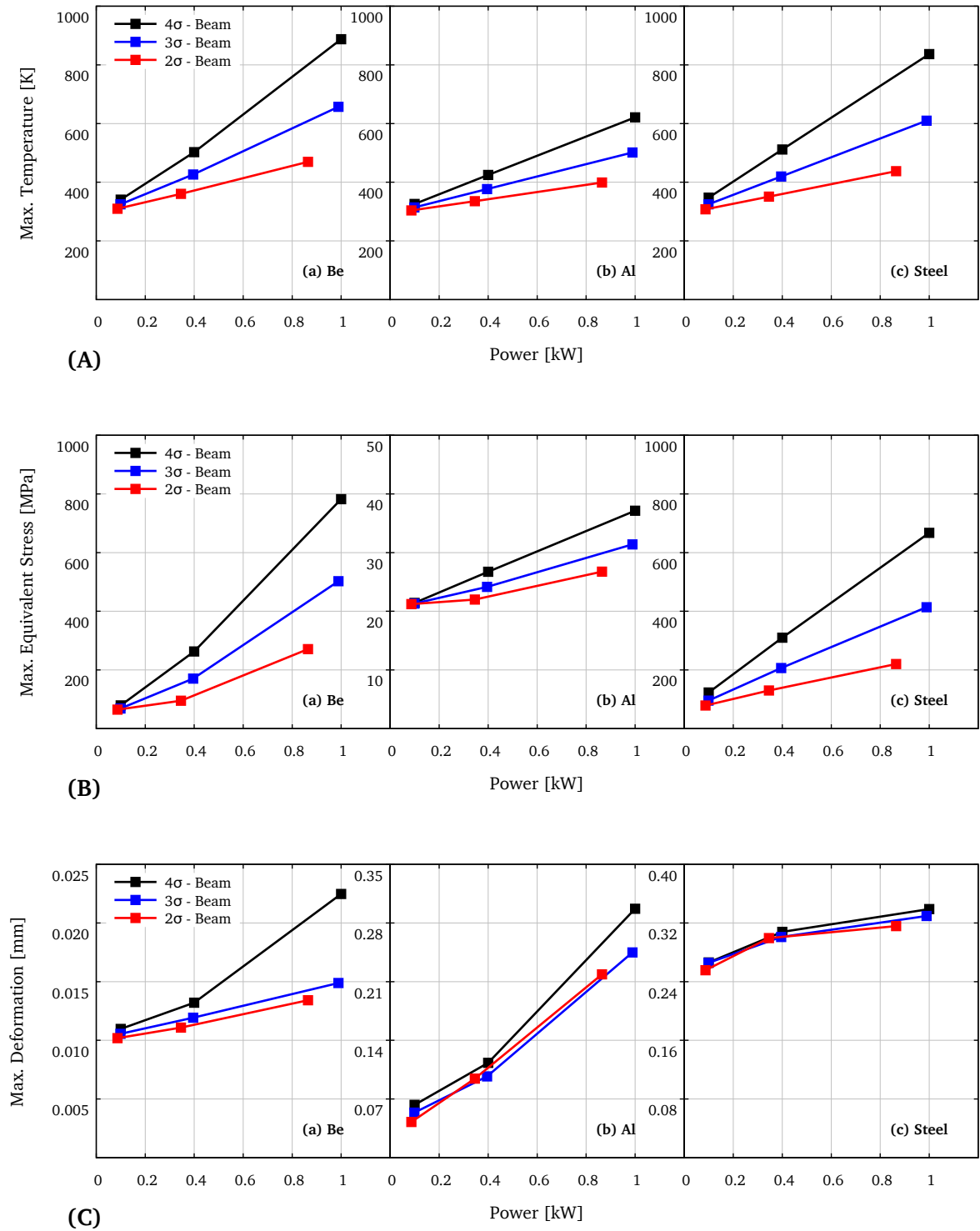


Figure 4.2: Maximum temperature, stress, and deformation values reached within the target materials, for varying beam power and beam profiles.

Table 4.2: Results of the simulations for varying beam power and beam profiles.

Beam Power [kW]	Material	Thickness [mm]	4 $\sigma$ - beam			3 $\sigma$ - beam			2 $\sigma$ - beam		
			T <sub>max</sub> [K]	D <sub>max</sub> [mm]	S <sub>max</sub> [MPa]	T <sub>max</sub> [K]	D <sub>max</sub> [mm]	S <sub>max</sub> [MPa]	T <sub>max</sub> [K]	D <sub>max</sub> [mm]	S <sub>max</sub> [MPa]
0.10	Steel	0.235	347	0.266	123	325	0.266	96	308	0.256	79
	Al	0.581	326	0.063	21	314	0.054	21	304	0.043	21
	Be	0.700	341	0.011	79	325	0.011	79	310	0.010	75
0.40	Steel	0.235	511	0.308	310	420	0.301	207	351	0.299	130
	Al	0.581	425	0.113	27	376	0.097	24	335	0.094	22
	Be	0.700	503	0.013	263	426	0.012	170	360	0.011	95
1.00	Steel	0.235	837	0.339	667	610	0.329	414	438	0.316	220
	Al	0.581	621	0.297	37	501	0.245	31	399	0.219	27
	Be	0.700	888	0.023	782	657	0.015	502	470	0.013	271
2.50	Steel	0.235	1656	0.418	1568	1087	0.404	934	654	0.345	442
	Al	0.581	1115	0.669	52	814	0.605	47	558	0.573	36
	Be	0.700	2195	0.080	2504	1377	0.040	1510	773	0.016	763
5.00	Steel	0.235	3018	0.545	3150	1876	0.503	1789	1015	0.417	817
	Al	0.581	1935	1.298	63	1335	1.241	57	822	1.087	48
	Be	0.700	4237	0.184	5217	2716	0.119	3368	1374	0.033	1707

T<sub>max</sub>: max. temperature in target

D<sub>max</sub>: max. deformation in target

S<sub>max</sub>: max. stress in target

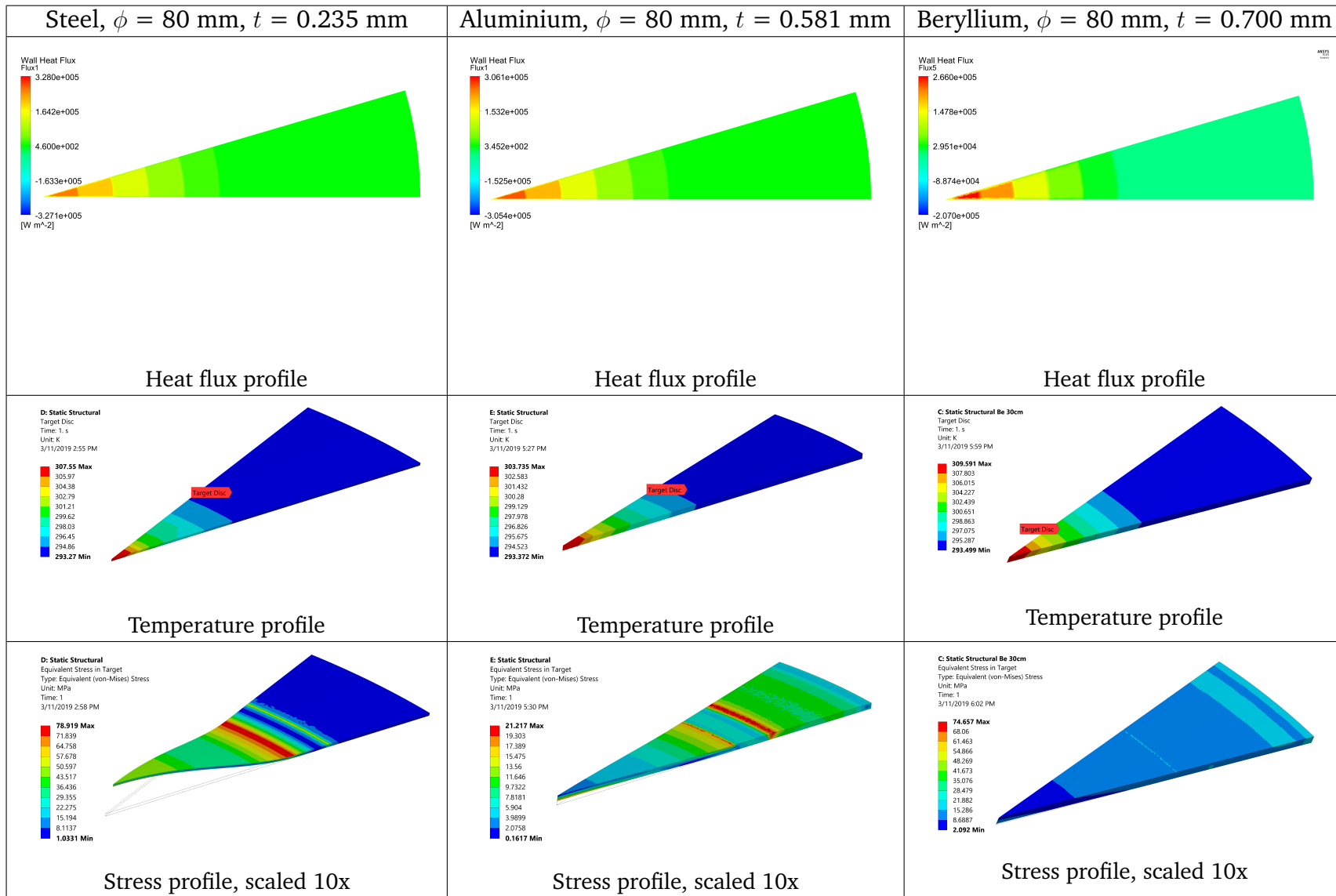


Figure 4.3: Results of the simulations for Be, Al, and Steel targets subjected to a beam power of 0.1 kW (beam spot,  $\phi = 30$  mm, corresponds to  $[-2\sigma:2\sigma]$ ).

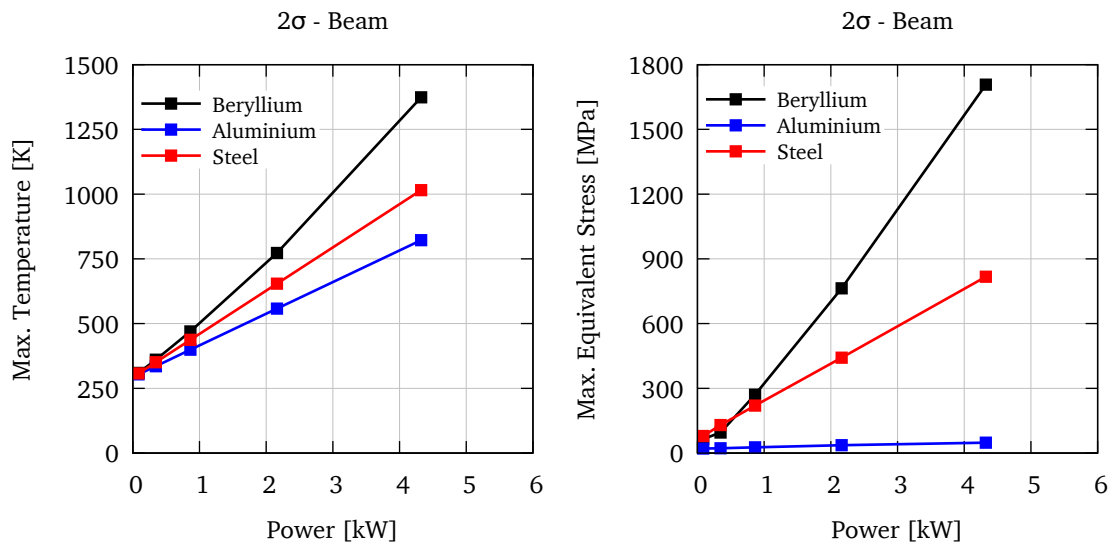


Figure 4.4: Maximum equivalent stress and temperature values for different materials, resulting from a  $2\sigma$  - beam operated at 0.1 kW.

## Chapter 5

# Setup of the Target-Test-Station

### 5.1 General Description

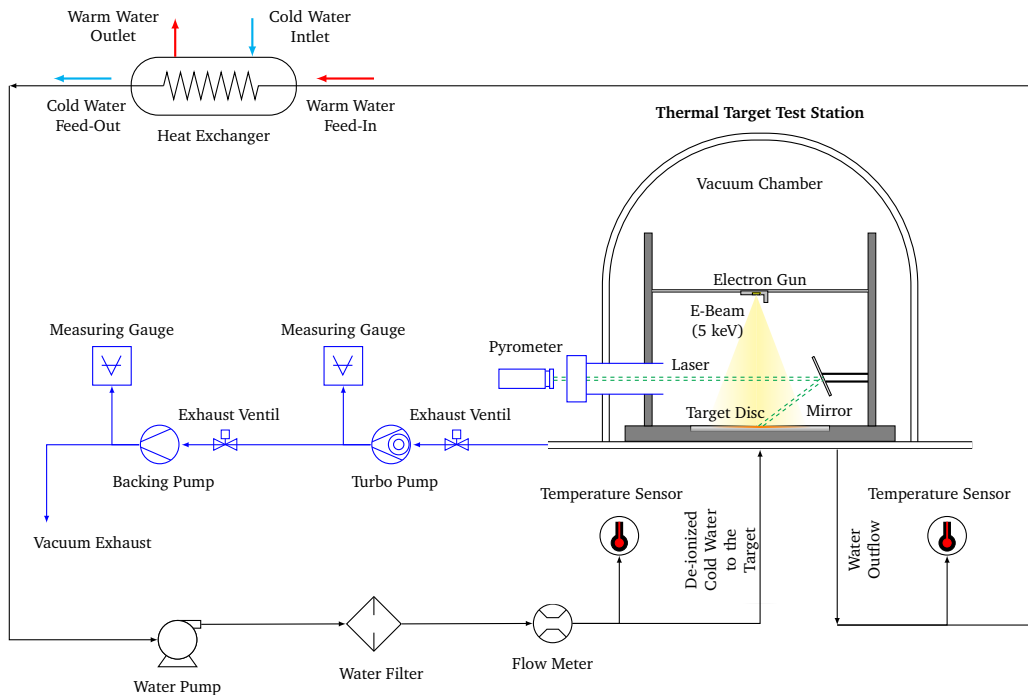


Figure 5.1: Schematic of the thermal-target-test station.

Figure 5.1 shows the general schematic of the setup constructed and developed during this work. The setup can be broken down into three main sub-groups:

- i the main vacuum chamber, along with the e-gun and the target disc;
- ii the electrical power supply for the e-gun; and

iii the external water cooling channel.

The vacuum chamber (consists of the vacuum vessel, a glass cover, and instrumentation) is evacuated by two vacuum pumps (a backing pump and a secondary turbo pump connected serially). The pumps in combination have a capacity to produce a vacuum in the order of  $10^{-7}$  mbar. There are three main reasons to use vacuum conditions for the setup.

Firstly, the impinging electron beam will lead to elevated temperatures of a few 100 °C at the target surface, and since many metals, including aluminium and iron, oxidize or even burn at such high temperatures under standard atmospheric conditions, it is crucial to avoid such instances. Secondly, the presence of air molecules hinders the path of the electrons, causing a loss in the power delivered to the target and wastage of the input energy. Lastly, the electron gun accelerates the electrons to obscenely fast speeds via electrostatic potential difference (max.  $\sim 10$  kV) between the accelerating electrodes ( $\sim 2$  cm apart). This results in an enormous electric field gradient between the electrodes, and thus, the setup must remain evacuated to avoid electric sparks.

The vacuum vessel has the targetry for the NOVA ERA installed at its base. For the initial investigations, a steel disc is used as the prime target (rather than the actual Be-disc). For the reason that steel offers a much better mechanical stability, it is pragmatic to run the first tests with it. Also, beryllium is a toxic material and must be handled with extra caution, when worked with. Thus, testing the setup with steel first (and later aluminium) can deliver assurance of the safe operation of the setup before beginning actual tests with Be, and ultimately, the rest of the HBS target materials (V, Ta, W, etc.). The vacuum vessel also comprises of an externally mounted pyrometer to monitor and report target surface temperatures, while in operation.

An external heat removal water cooling channel also exists below the target to continuously cool down the target. As shown in [Figure 5.1 on the preceding page](#), the cold water is pumped to the target, and the warm water is directed to an heat exchanger, which again feeds the cold water back to the water pump. Using an ultrasonic flow meter, the mass flow of the water to the target disc is also monitored.

## 5.2 Pyrometer Calibration

As mentioned in Section 3.4 on page 31, the prime technique used to measure target (surface) temperatures in this work is *radiation pyrometry*. A digital pyrometer, **PYROSPOT DPE 10M** (see Figure 5.2), by *DIAS Infrared Systems* is, thus, employed with the technical specifications, as listed in Table 5.1. The applicability of such a device is, however, only as good as the knowledge of emissivity of surfaces that are to be probed (see Section 3.4.1.2 on page 36).

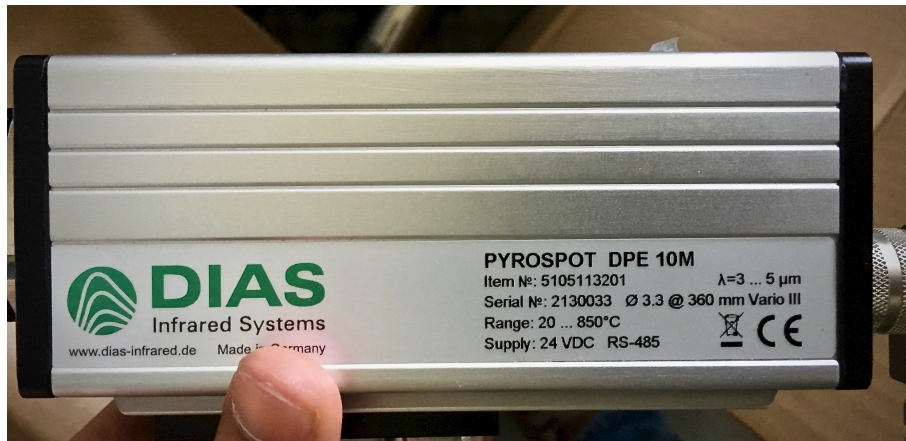


Figure 5.2: PYROSPOT DPE 10M by DIAS Infrared Systems used to measure surface temperatures.

Table 5.1: Technical data for PYROSPOT DPE 10M. [67]

Specification	Description
Temperature range	20 °C - 850 °C
Operating temperature	0 °C - 70 °C
Spectral range (detection window)	3.0 μm - 5.0 μm
Measurement uncertainty	up to 400 °C: 2 K; above 400 °C: 1 K
Response time	1.5 ms, adjustable up to 100 s

The inherent complexity in determining the emissivity of given target materials puts a limitation on the efficacy of pyrometric temperature measurements. From

Equation 3.15, it is known that an ideal black body exhibits perfect emissivity, i.e.,  $\varepsilon(\lambda) = 1$ . In all other cases, the emissivity is a function of many optical and surface characteristics of the given material as well as the temperature of the measured body (see Figure 5.3).

Therefore, in order to get a calibrated temperature reading, the emissivity is required to be changed with the change in temperature of the target. As this is impracticable, it is better to fix the emissivity to a specific value, e.g.  $\varepsilon(\lambda) = 1$ , and to measure the the temperature with a second calibrated temperature reading instrument (a thermocam in this case). Thus, by correlating the temperature values of the two devices, the pyrometer can be easily calibrated.

However, this holds true only, if the emissivity is not wavelength dependent, i.e., the emissivity is constant at all wavelengths, which is also the case with most polished and smooth metallic surfaces (see Section 3.4.1.2 on page 36). For the purposes of this work, it is safe to assume that the target metal discs are all pure metals (or pure metallic alloys) with clean and smooth surfaces. This already eliminates any surface and wavelength dependencies of emissivity.

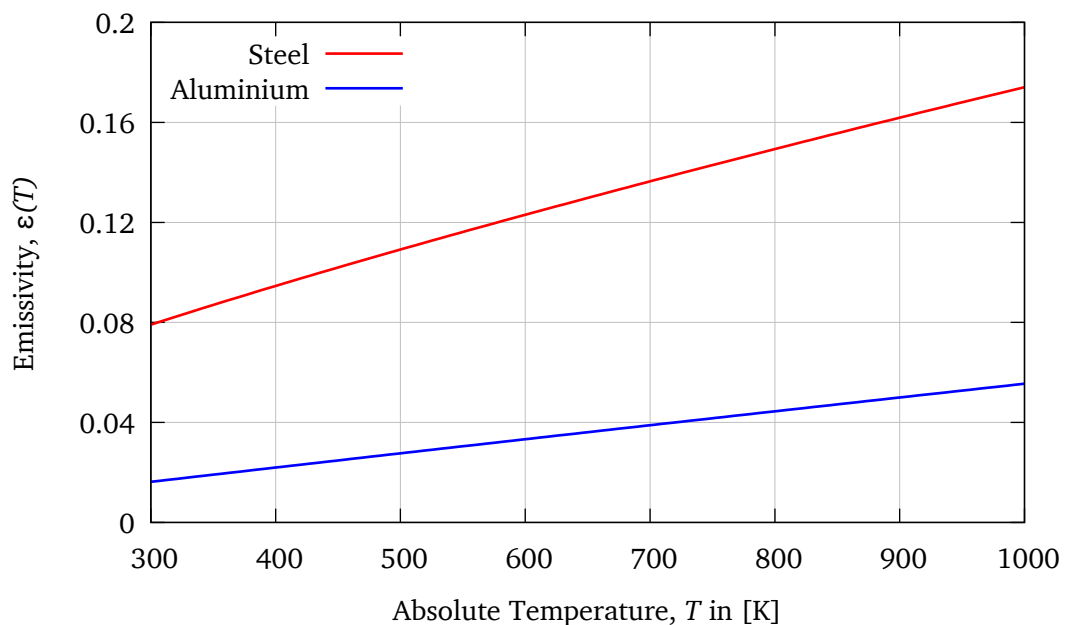


Figure 5.3: Emissivity as a function of temperature for Steel and Aluminium, calculated theoretically according to Equation 3.18. In the temperature range expected to be reached during the experiments, the emissivity for both Aluminium and Steel exhibits a linear temperature dependence.

The emissivity, however, still depends on the temperature, which from Equation 3.18 is a linear function of the temperature, if the observed temperature range is not too large, as shown in Figure 5.3 [64].

Since a true temperature measurement can only result, if the employed equipment is well calibrated against a standard reference and all plausible uncertainties and errors are taken into account, it is achieved by carefully designing a setup that is efficient and reproducible.

Figure 5.4 shows the implemented setup for pyrometer calibration. The setup consists of

- i the vacuum vessel with the target disc set in its position;
- ii optical mirror mounted on a goniometer stage (movable in all directions);
- iii the PYROSPOT pyrometer aimed at the target surface through the sapphire glass window (via the mirror);
- iv the thermocam looking down at the target through air; and
- v a heating plate ( $\sim 250$  °C), placed below the target-test-station.

The sapphire glass (crystallized  $\text{Al}_2\text{O}_3$ ) displays a particularly high transmittance ( $\sim 0.85$ ) in the MWIR region (see Section 3.4.2 on page 37), acting almost transparent to the pyrometer. The target disc is half black coated, causing it to furnish emissivity close to one. The thermocam focuses on the black part, while the pyrometer is directed at the non-coated part.

### 5.2.1 Calibration Curves

Figure 5.5 shows the measured temperature values from the pyrometer vs. the actual temperature values of the black-coated target surface from the thermocam. The measured calibration curves are for Steel and Aluminium, for which the initial experiments are planned to be carried out. From the curves, it is also evident that the pyrometer measures lower temperatures than actual, which is also anticipated, since the non-coated surface corresponds to lower emissivity values.

As the pyrometer is already calibrated in the exact configuration it will be used during the actual experiments, any uncertainties due to reflection or absorption by the mirror, angle of view, etc. are already compensated. Thus, by reading the pyrometer with the respective calibration curves, true measured temperature values can be discerned for both the materials.

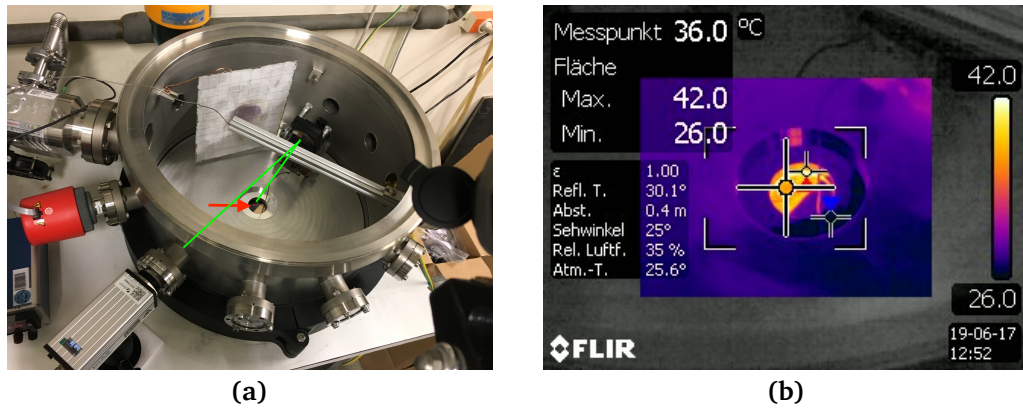


Figure 5.4: (a) The setup used to calibrate the pyrometer with the target disc coated half black to provide an emissivity of close to 1. The pyrometer looks through a sapphire crystal glass window onto the target via a mirror with high reflectivity. (b) A thermal image of the target being heated up, via a calibrated thermocam. The thermal image shows regions of maximum and minimum temperatures at the target surface.

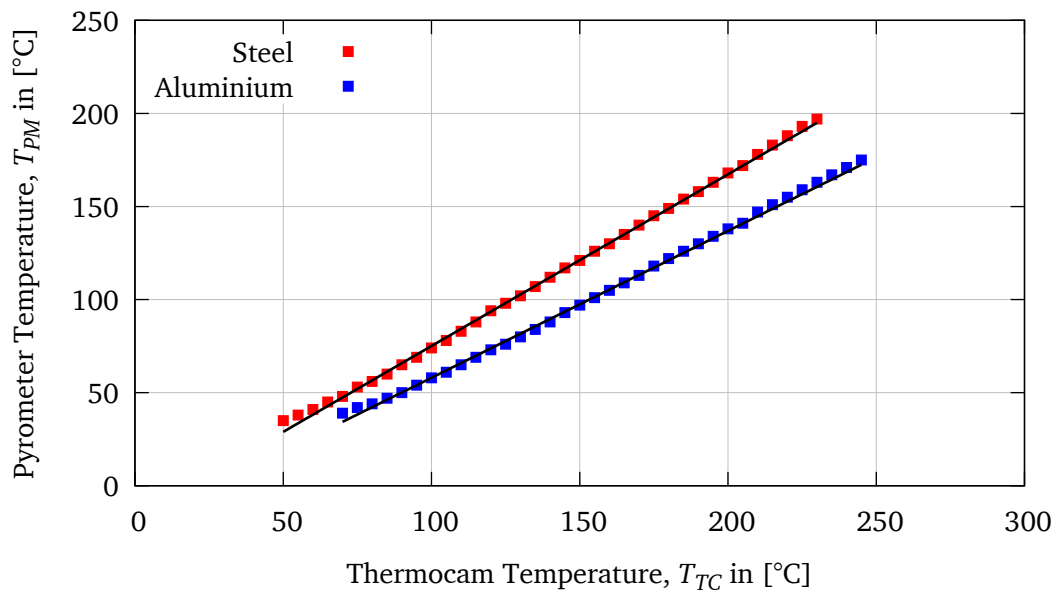


Figure 5.5: Calibration curves for the pyrometer for Steel and Aluminium.

From Figure 5.5, the linear fits to the measured sets of data points give for Aluminium and Steel the following functions

$$T_{PM,Al} = 0.922 \cdot T_{TC,Al} - 17.158 \quad (5.1)$$

and

$$T_{PM,Steel} = 0.789 \cdot T_{TC,Steel} - 20.928, \quad (5.2)$$

where all temperature values are given in [°C]. With these equations, the real temperatures can be calculated for Steel and Aluminium. For other target materials, new calibration curves need to be determined.

### 5.3 E-Beam Collimation

The geometry of electron emission of the e-gun used in the work must be known, before any actual experimental measurements can be performed. This requires a stable method to detect the beam, while simultaneously giving information about the cross-sectional shape or profile of the beam perpendicular to its direction of propagation. This is realized by coating a thick steel plate with a supersaturated solution of common salt (NaCl) and water.

The water upon evaporation leaves behind a crystallized NaCl coating on top of the plate, which serves as a scintillating material for the electrons. Every time a fast enough electron hits this coating, it causes electrons to transition to higher orbitals in the elements. Upon de-excitation, a photon is released in the visible spectrum of the EM-radiation, making the beam spot on the plate visible to the naked eye.

The plate is also equipped with a wire grating with horizontal and vertical spacing of 2 cm. This provides a facile estimation of the beam spot size on the plate, allowing for an elementary way to estimate the beam shape and size.

The plate is then screwed to a movable pin, that can translate the plate back and forth via an external rotational knob. This facilitates the adjustment of distance relative to the e-gun, thus, allowing a distance dependent beam characterization, as shown in Figure 5.6.

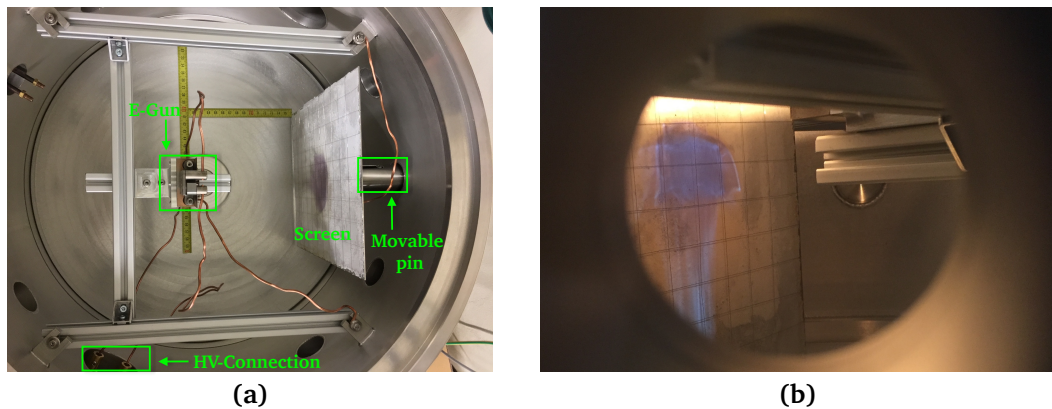


Figure 5.6: (a) Setup inside the vacuum vessel to measure the beam profile. (b) First measurement without any focusing electrodes. This shape, as anticipated, is broad and rectangular with a considerable downward deflection of the beam.

Figure 5.6 also illustrates the beam profile without any modifications to the e-gun. In the absence of any focusing elements, the electron emission from the cathode corresponds to the filament's cross-sectional geometry, i.e., a rectangular form. Since there is no focusing arrangement in this case, the beam broadens out significantly in a very short distance ( $\sim 12$  cm), spanning almost half of the screen-width ( $\sim 19$  cm).

The beam also exhibits a vertical tail on the lower part of the screen. This deflection is speculated to be a result of the asymmetry of the setup inside the vacuum vessel itself and especially due to an off-centered cathode. Consequently, a part of the beam is deflected downwards. Yet another factor influencing this behaviour could be the cavity profile on the anode (rectangular in this case with dimensions: 16 mm x 9 mm). Since the geometrical configuration in the initial design of the e-gun is such that the lower most cavity edge on the anode aligns horizontally with the cathode filament, it could also result in the beam being deflected in the downward direction.

An initial disclosure of the working e-gun already puts some challenges on achieving a beam profile that can be later made usable for experiments, in an ideal scenario—a *circular gaussian* profile.

A series of improvement steps were then accordingly drawn out and undertaken as means to fine tune and ultimately to collimate the beam. In the first instance,

different anodes with varying cavity profiles were employed separately and later in combination of two, with one acting as a wehnelt electrode and the other as an anode, in order to understand the behaviour of beam in relation to the shape of the electrode cavities as well as to refine the beam profile. Additionally, this was done to qualitatively determine the best possible configuration for the e-gun's operation.

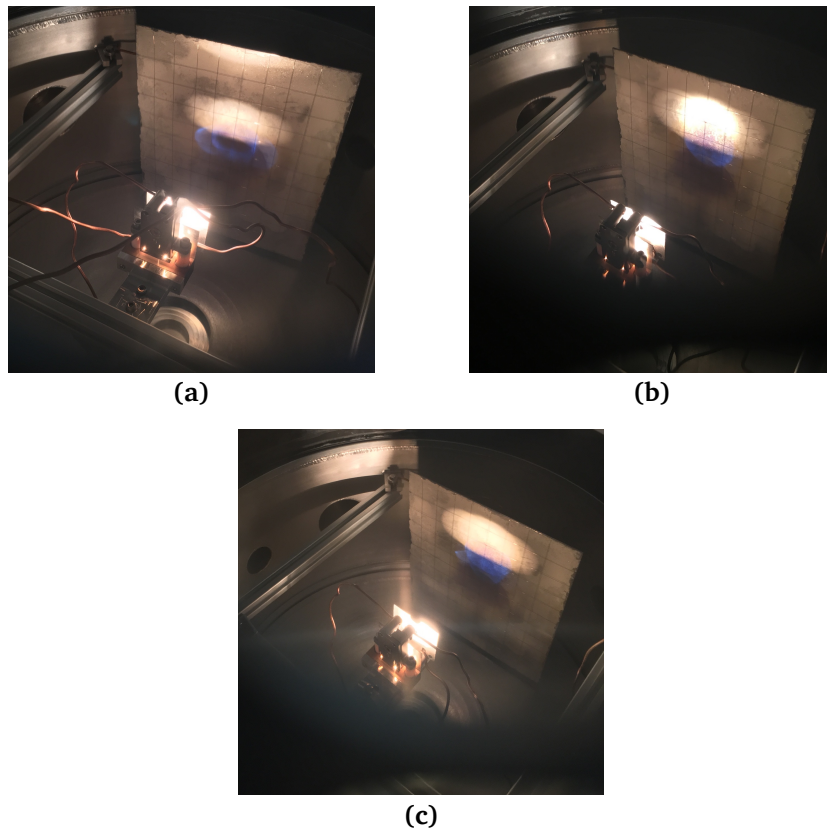


Figure 5.7: Effect of the electrodes' shapes and combinations on the beam profile. (a) With two circular cavity profiles of different radii, (b) with an oval and a circular cavity profile, and (c) with a rectangular and a circular cavity profile on the two electrodes, respectively.

Figure 5.7 displays the varied combinations tested and their respective effects on the beam profile. As can be evidently seen, Figure 5.7 (b) shows the closest to a circular shaped beam. This clearly indicates a better combination to be pursued and improved upon.

As a next step, different high voltage (HV) values were applied to the electrodes to collimate the beam, however, in some cases an overloading issue was faced. It was then decided to leave the primary electrode (wehnelt) floating (non-grounded

without any external applied HV). The working theory behind this concept is that the electrons impinging on the primary electrode accumulate on it (charge deposition) over time, and since there is no way for them to flow out, the electrode reaches a saturation with respect to the incoming electron beam current, and thus, self-regulates to provide a focusing potential. This squeezes the incoming electrons, as they pass through the oval cavity of this electrode, accelerating towards the anode.

The final configuration of the e-gun used in the work that provides a workable beam profile, although not a gaussian distribution, is shown in Figure 5.8.

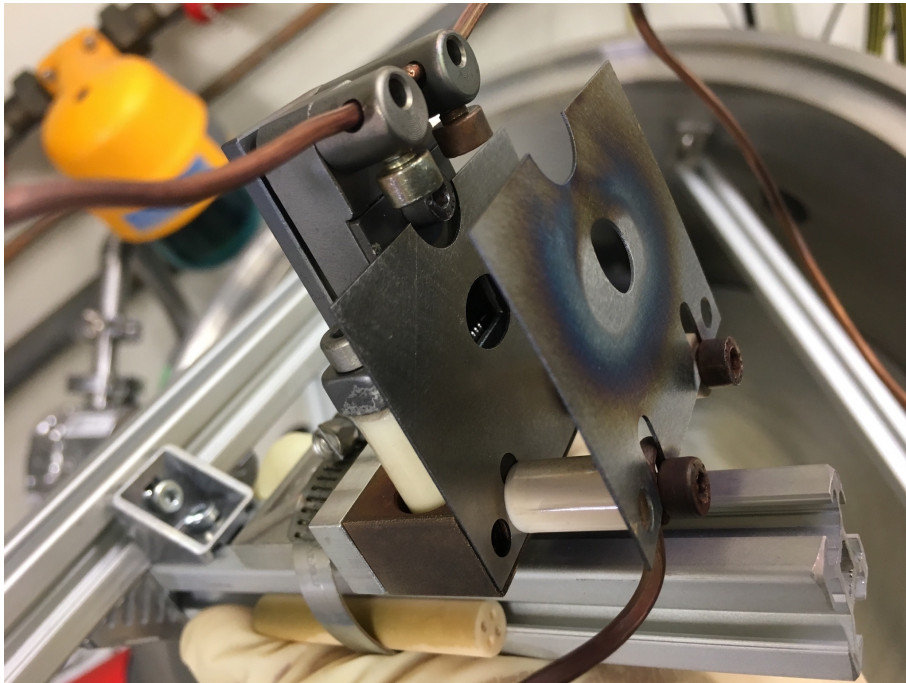


Figure 5.8: The e-gun configuration used in this work with a primary oval cavity wehnelt electrode (floating) and a secondary circular cavity anode at HV.

## 5.4 E-Beam Characterization and Optimization

The next task is to properly measure and characterize the beam spot size, which must be less than a circle of 30 mm diameter as per the requirement of the target geometry for the NOVA ERA (see Section 2.3.2 on page 16). Since the beam profile does not really correspond to a circular gaussian shape, a set of parametric mathematical equations are rather used to approximately characterize the beam profile. The set of mathematical functions are chosen arbitrarily such that they best

fit the shape of the beam spot, as shown in Figure 5.9. The mathematical functions are described in detail in Appendix 6.

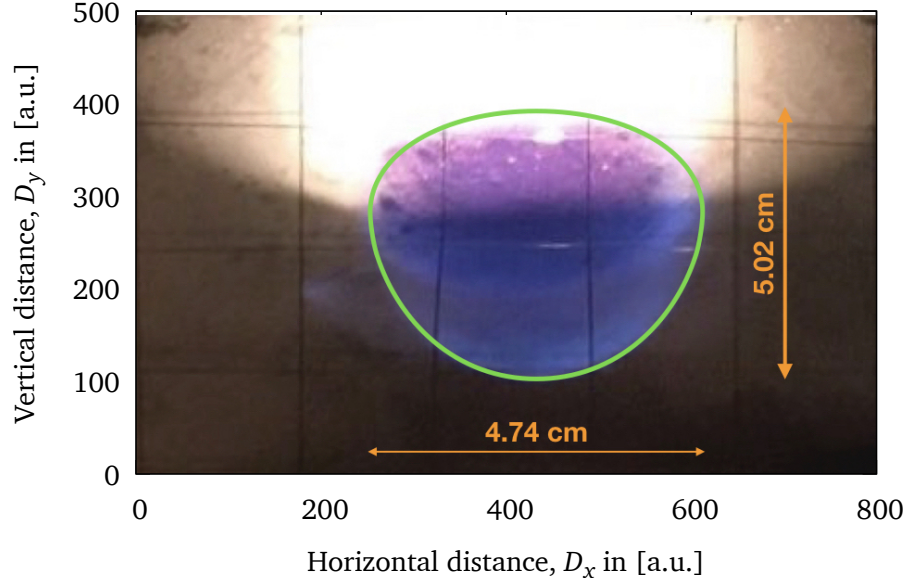


Figure 5.9: The beam spot is circumscribed by a green curve, which is a close approximation of the beam profile, as described by equations 5.3 and 5.4.

For any such beam spot, the set of mathematical functions using Equation A3.6 can be determined via the spot width and height. Thus, the individual sets of equations for the beam spot in Figure 5.9 are:

$$\begin{aligned} x_1 &= 0.754 \cdot (t - \sin t) - 2.37 \text{ \& } \\ y_1 &= 0.837 \cdot (1 - \cos t) , \end{aligned} \quad (5.3)$$

and

$$\begin{aligned} x_2 &= 0.754 \cdot (t - \sin t) - 2.37 \text{ \& } \\ y_2 &= -1.673 \cdot (1 - \cos t) , \end{aligned} \quad (5.4)$$

with the total area given by Equation A3.7 as:

$$A = 3 \cdot \pi \cdot 0.754 \cdot (0.837 + 1.673) = 17,84 \text{ cm}^2 , \quad (5.5)$$

and by Equation A3.8 as:

$$A = \pi \cdot \left( \frac{4.74 + 5.02}{2} \right)^2 = 18,70 \text{ cm}^2, \quad (5.6)$$

which are in good agreement with each other, substantiating that both the approaches are suitable to make a reliable estimate of beam spot area. As argued in Appendix 6, the latter approach is employed to also account for the area of the beam spots, which could not be photographed due to space limitations of the setup as well as the viewing opening of the flange.

To correlate the beam collimation and the distance of the e-gun to the scintillation plate, a series of beam profiles were acquired, by moving the plate away from to the e-gun in steps, starting from an initial distance of 23.50 cm. For each measurement, the beam size (width and height) and the distance of the plate from the e-gun were recorded. The beam spot area, approximated using Equation A3.8, is then plotted against the corresponding distance, as shown in Figure 5.10. The graph reveals the correlation to be an inverse square function, with the beam size achieving a minimum at about 35 cm. This also demonstrates that under the given setup, achieving a narrower beam spot size is not practically possible.

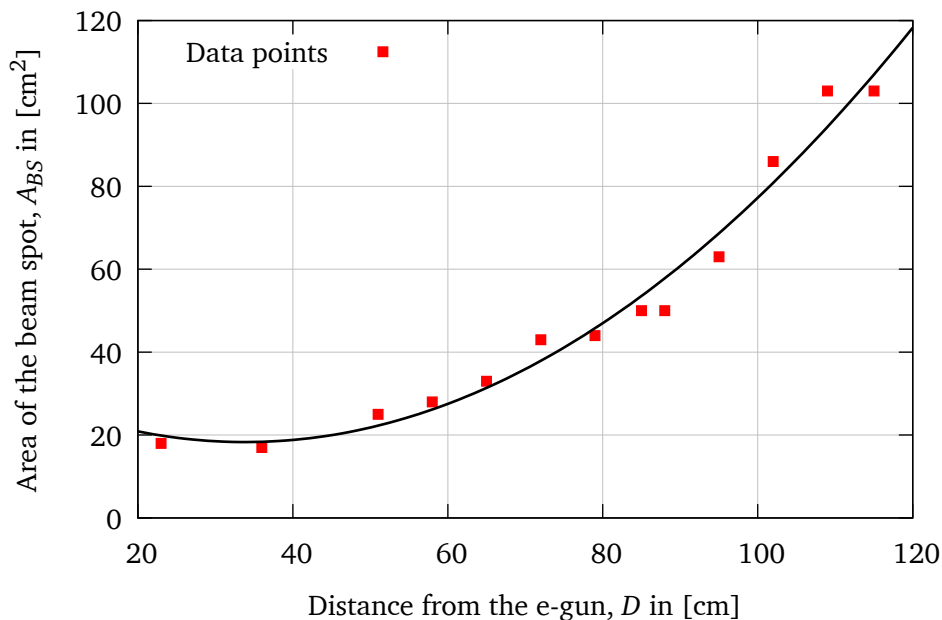


Figure 5.10: The beam profile characterization with respect to the distance from the e-gun, showing an inverse squared dependence.

# Conclusions

---

This work attempts to lay the groundwork for the development of the target test station, which will be used to carry out target material investigations in the framework of the HBS project. The major advantage of such a setup comes from the fact that it utilizes low energy electron beams (upto 10 keV) to correlate the thermo-mechanical effects that are expected to be induced by proton beams of relatively higher energies (upto 100 MeV). The method, thus, offers the practicality of designing and setting up an experimental workbench in a laboratory space, contrary to working with a proton (or deuteron) accelerator.

The work is carried out in two main parts:

- i the thermo-mechanical ANSYS simulation studies; and
- ii the setting up of the main experimental test station.

The simulation studies elucidates the thermal and structural deformations undergone by the target disc due to the impinging electron beam at various beam powers and profiles. It summarizes the thermo-mechanical ANSYS simulation analysis for three different target materials (Be, Al, and Steel). The material layer thickness was adjusted according to the proton range of a 10 MeV beam exiting the material at 2 MeV.

It was shown that the heat deposition due to low energy electron beam greatly depends on the beam profile, and that a more spread-out beam is suitable to prevent localized heating in the target, leading to high temperatures and stresses. At the same time, with a broader beam, the average power transferred to the target also decreases. Therefore, an optimum must be found out, so as to not lose

the beam power significantly, while also avoiding structural and thermal failures in the target during operation. This was determined to be a  $2\sigma$  - beam on the target, transferring a thermal load of  $\sim 86\%$  of the actual beam power to the target.

The second part of the thesis, aimed to develop the thermal-target-test station, involved two main sub-parts: (a) characterizing the radiation pyrometer to acquire non-contact surface temperature of the target discs; and (b) configuring, focusing, and characterizing the e-gun to achieve a quasi-homogeneous beam profile. The electron beam was shaped and focused electrostatically, i.e. without magnets, to save space inside the vacuum vessel and to allow easy maneuvering of the e-gun within the vessel.

This work provides a good understanding of the challenges involved in fully characterizing the target materials with the thermal-target-test station and the developmental work to bring the experimental setup in a functional capacity. However, still improvements can be done to the simulation model, once good experimental results exist, which can allow to further optimize the beam profile parameters.

A better electron gun is suggested to be introduced, replacing the one used in the work, with dedicated focusing elements to achieve a better quality gaussian beam.

The overall work, within the scope of this thesis, gives a qualitative description of the thermo-mechanical stress build-ups and the associated deformations in the respective target materials along with the functional test setup that can be taken into operation for the first measurements with the electron beams.

# Appendix: 1

Table A1.1: Thermo-mechanical material properties of Beryllium (non-linear) [66].

Temperature	Mass Density	Avg. Tensile Strength	Avg. Yield Strength	Young's Modulus	Poisson's Ratio	Mean Thermal Expansion	Thermal Conductivity	Specific Heat
[°C]	[kg m <sup>-3</sup> ]	[MPa]	[MPa]	[GPa]	[-]	[10 <sup>-6</sup> K <sup>-1</sup> ]	[W m <sup>-1</sup> K <sup>-1</sup> ]	[J kg <sup>-1</sup> K <sup>-1</sup> ]
20.00	1830.00	387.00	249.00	306.00	0.10	11.56	200.00	1807.00
100.00	1825.00	361.00	236.00	303.00	0.10	12.51	169.00	2046.00
200.00	1817.00	324.00	216.00	299.00	0.10	13.51	144.00	2295.00
300.00	1808.00	284.00	193.00	294.00	0.10	14.32	127.00	2497.00
400.00	1799.00	240.00	168.00	288.00	0.10	14.96	116.00	2660.00
500.00	1789.00	191.00	140.00	281.00	0.10	15.60	107.00	2791.00
600.00	1779.00	139.00	109.00	273.00	0.10	15.85	100.00	2998.00
<b>Melting Point</b>	<b>1551.15 K</b>							

Table A1.2: Thermo-mechanical material properties of Aluminium (non-linear) [66].

Temperature	Mass Density	Avg. Tensile Strength	Avg. Yield Strength	Young's Modulus	Poisson's Ratio	Mean Thermal Expansion	Thermal Conductivity	Specific Heat
[°C]	[kg m <sup>-3</sup> ]	[MPa]	[MPa]	[GPa]	[-]	[10 <sup>-5</sup> °C <sup>-1</sup> ]	[W m <sup>-1</sup> K <sup>-1</sup> ]	[J kg <sup>-1</sup> K <sup>-1</sup> ]
20.00	2700.00	47.384	31.174	69.076	0.35	2.3189	237.00	893.92
100.00	2684.40	42.190	29.717	66.275	0.35	2.3628	240.00	942.89
200.00	2664.00			62.487	0.35	2.4277	237.00	985.97
300.00	2642.20			57.291	0.35	2.5330	233.00	1028.05
400.00	2618.60			49.758	0.35	2.6474	116.00	1069.13
500.00	2593.10			35.574	0.35	2.7479		
600.00	2569.20				0.35	2.8614		
<b>Melting Point</b>	<b>933.52 K</b>							

Table A1.3: Thermo-mechanical material properties of Steel (linear).

Temperature	Mass Density	Avg. Tensile Strength	Avg. Yield Strength	Young's Modulus	Poisson's Ratio	Mean Thermal Expansion	Thermal Conductivity	Specific Heat
[°C]	[kg m <sup>-3</sup> ]	[MPa]	[MPa]	[GPa]	[-]	[10 <sup>-5</sup> °C <sup>-1</sup> ]	[W m <sup>-1</sup> K <sup>-1</sup> ]	[J kg <sup>-1</sup> K <sup>-1</sup> ]
<i>All Temp.</i>	7850.00	460.00	250.00	200.00	0.30	1.20	54.00	490.00
<b>Melting Point</b>	<b>1643.15 K</b>							

---

## Appendix: 2

---

Probability density function of a 2D circular symmetric Gaussian distribution.

Let  $G^2(x, y)$  be a general 2D Gaussian distribution function, such that

$$G^2(x, y) = \frac{1}{\sqrt{2 \cdot \pi} \cdot \sigma_x} \cdot \frac{1}{\sqrt{2 \cdot \pi} \cdot \sigma_y} \cdot e^{-\left(\frac{(x - \mu_x)^2}{2 \cdot \sigma_x^2} + \frac{(y - \mu_y)^2}{2 \cdot \sigma_y^2}\right)}, \quad (\text{A2.1})$$

where

$\sigma_x$  is the standard deviation in  $x$ ;  
 $\sigma_y$  is the standard deviation in  $y$ ;  
 $\mu_x$  is the expectation of  $x$ ; and  
 $\mu_y$  is the expectation of  $y$ .

For a symmetric Gaussian distribution centered at the origin  $O(0, 0)$ ,  $G^2(x, y)$  reduces to the form

$$G^2(x, y) = \frac{1}{2 \cdot \pi \cdot \sigma^2} \cdot e^{-\left(\frac{x^2 + y^2}{2 \cdot \sigma^2}\right)}, \quad (\text{A2.2})$$

where

$\sigma_x = \sigma_y = \sigma$ ; and  
 $\mu_x = \mu_y = 0$ .

The probability density function,  $P(\{x, y\} | \sigma^2)$ , of this Gaussian distribution in some arbitrary closed interval  $x \in [-a, a]$  and  $y \in [-a : a]$  is then

$$P(\{x, y\} | \sigma^2) = \int_{-a}^{+a} \int_{-a}^{+a} G^2(x, y) \cdot dx \cdot dy . \quad (\text{A2.3})$$

The above integral can then be evaluated easily by transforming the system into polar coordinates, over the whole  $2\pi$  domain. Thus, Equation A2.3 becomes

$$P(\{R, \theta\} | \sigma^2) = \int_0^{2\pi} \int_0^R r \cdot G_p^2(r, \theta) \cdot dr \cdot d\theta , \quad (\text{A2.4})$$

where

$$G_p^2(r, \theta) = \frac{1}{2 \cdot \pi \cdot \sigma^2} \cdot e^{-\left(\frac{r^2}{2 \cdot \sigma^2}\right)} \quad \text{and}$$

$$R = \sqrt{(a^2 + a^2)} = \sqrt{2} \cdot a.$$

Equation A2.4 can be solved in the following manner

$$\begin{aligned}
P(\{R, \theta\} | \sigma^2) &= \int_0^{2\pi} \int_0^R r \cdot \frac{1}{2 \cdot \pi \cdot \sigma^2} \cdot e^{-\left(\frac{r^2}{2 \cdot \sigma^2}\right)} \cdot dr \cdot d\theta \\
&= [\theta]_0^{2\pi} \cdot \int_0^R r \cdot \frac{1}{2 \cdot \pi \cdot \sigma^2} \cdot e^{-\left(\frac{r^2}{2 \cdot \sigma^2}\right)} \cdot dr \\
&= [2\pi - 0] \cdot \frac{1}{2 \cdot \pi \cdot \sigma^2} \cdot \int_0^R r \cdot e^{-\left(\frac{r^2}{2 \cdot \sigma^2}\right)} \cdot dr \\
&= [2\pi] \cdot \frac{1}{2 \cdot \pi \cdot \sigma^2} \cdot \left[ -\sigma^2 \cdot e^{-\left(\frac{r^2}{2 \cdot \sigma^2}\right)} \right]_0^R \\
&= - \left[ e^{-\left(\frac{r^2}{2 \cdot \sigma^2}\right)} \right]_0^R \\
&= - \left[ e^{-\left(\frac{R^2}{2 \cdot \sigma^2}\right)} - e^{-\left(\frac{0^2}{2 \cdot \sigma^2}\right)} \right] \\
&= \left[ e^{-\left(\frac{0^2}{2 \cdot \sigma^2}\right)} - e^{-\left(\frac{R^2}{2 \cdot \sigma^2}\right)} \right] \\
\Rightarrow P(\{R, \theta\} | \sigma^2) &= \left[ 1 - e^{-\left(\frac{R^2}{2 \cdot \sigma^2}\right)} \right] \\
&\text{or simply,} \\
P(\{R\} | \sigma^2) &= \left[ 1 - e^{-\left(\frac{R^2}{2 \cdot \sigma^2}\right)} \right]. \tag{A2.5}
\end{aligned}$$

Since the whole  $2\pi$  angular domain has been considered in evaluating the probability density, it is justified to attribute only  $R$  as an independent variable to the function,  $P(\{R\} | \sigma^2)$ . Equation A2.5 can then be used to calculate probability densities for such a 2D gaussian distribution between any set of closed intervals, as shown in Table A2.4.

The resulting expectation values correspond to the average fraction of such a normalized 2D gaussian distribution in the respective  $\sigma$  ranges. This is then used to segment the beam spot region into concentric circular regions (see Figure 4.1), with each region accommodating the equivalent fraction of the total heat flux deposited at any given beam power at the target, thus, creating 2D stepwise gaussian heat flux profile associated with the electron beam.

Table A2.4: The expectation values corresponding to the defined  $\sigma$  ranges.

$\sigma$ -Values	Range	Expectation Value (from $P(\{R\}   \sigma^2)$ )
0.5	$-0.5\sigma - 0.5\sigma$	0.118
1.0	$-1.0\sigma - 1.0\sigma$	0.394
1.5	$-1.5\sigma - 1.5\sigma$	0.675
2.0	$-2.0\sigma - 2.0\sigma$	0.865
2.5	$-2.5\sigma - 2.5\sigma$	0.956
3.0	$-3.0\sigma - 3.0\sigma$	0.989
3.5	$-3.5\sigma - 3.5\sigma$	0.998
4.0	$-4.0\sigma - 4.0\sigma$	0.999

---

## Appendix: 3

---

The beam profile achieved with the employed e-gun deviates greatly from a circular gaussian distribution. While its shape cannot be empirically derived, a close mathematical approximation of the shape to characterize the beam profile is worked out.

It is assumed that the shape resembles a combination of two different irregular cycloids, sharing a common horizontal base. The general parametric equation of such a cycloid depends on the radius of a virtual moving circle with an arbitrarily chosen point on its circumference, whose motion traces the given cycloid. Then, for any such irregular cycloid  $C$ , the parametric equations are:

$$\begin{aligned}x &= a \cdot (t - \sin t) - c_x \text{ and} \\y &= b \cdot (1 - \cos t) - c_y.\end{aligned}\tag{A3.6}$$

For the beam profile, two such cycloids are needed, as shown in Figure A3.1 ( $C_1$  and  $C_2$ ), with a common horizontal base ( $a_1 = a_2 = a$  and  $c_{x1} = c_{x2} = c_x$ ). Depending on the acquired beam profile, the parameters  $a$ ,  $b_1$ ,  $b_2$ ,  $c_x$ ,  $c_{y1}$ , and  $c_{y2}$  are to be determined.

This simple approach of parameterizing the curve also results in the estimation of the beam area, since the area can simply be evaluated by integrating the area spanned by the curves, which results in the following

$$A = 3 \cdot \pi \cdot |a| \cdot (|b_1| + |b_2|).\tag{A3.7}$$

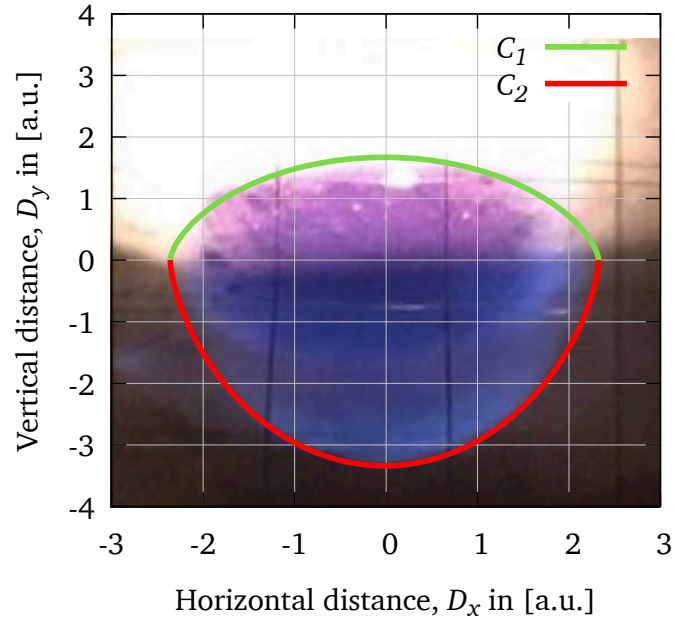


Figure A3.1: Mathematical approximation of the beam profile via a combination of two irregular cycloids,  $C_1$  and  $C_2$ , generated via Equation A3.6.

However, it was not possible to correctly photograph all the beam spots, due to the constrained setup of components in the vacuum chamber and restricted angle of viewing through the flange, a different approach for the determination of area of the beam spot was considered.

The area of the spot is, thus, estimated post the beam exposure using the beam impressions left on the scintillation screen. This is calculated using the area of circle with the radius equal to the mean of the width,  $D_x$ , and the height,  $D_y$ , of beam spot impression as follows

$$A = \pi \cdot \left( \frac{D_x + D_y}{2} \right)^2. \quad (\text{A3.8})$$

The approximated areas using Equations A3.7 and A3.8 are in good agreement with each other, as shown in Section 5.4 on page 62. Thus, Equation A3.8 is made use of to determine the areas of all beam spots, as illustrated in Figure A3.2, acquired within the framework of this thesis.

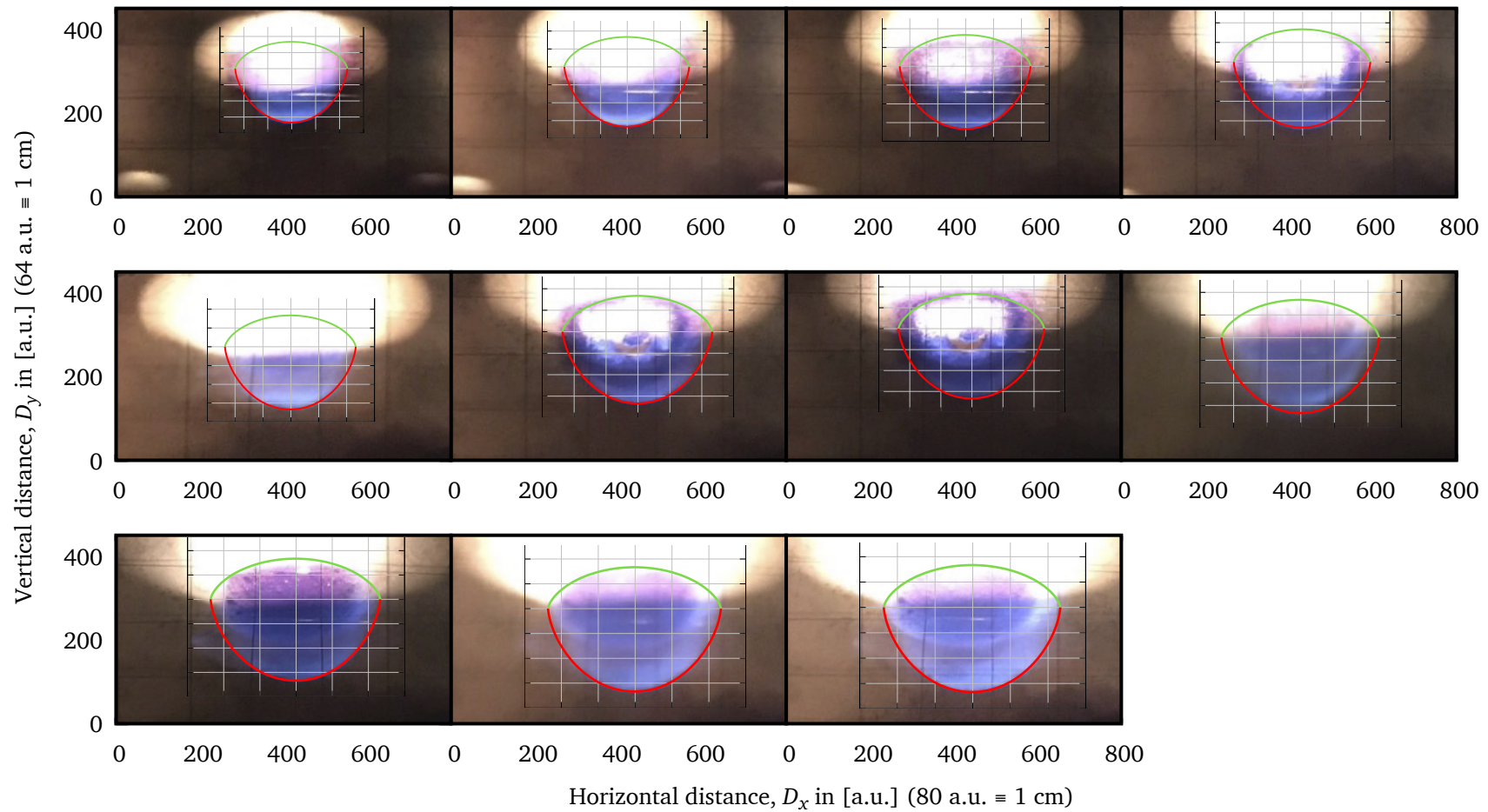


Figure A3.2: Photographed beam spots with corresponding encompassing beam profile curves. The beam spots are achieved by increasing distance between the e-gun and the screen.

---

# Bibliography

---

- [1] C. Carlile and C. Petrillo, “**Neutron scattering facilities in Europe: Present status and future perspectives,**” *ESFRI Report, European Landscape of Research Infrastructures-ESFRI*, p. 123, 2016.
- [2] T. Gutberlet, U. Rucker, P. Zakalek, T. Cronert, J. Voigt, J. Baggemann, P.-E. Doege, E. Mauerhofer, S. Böhm, J. Dabruck *et al.*, “**The Jülich high brilliance neutron source project—Improving access to neutrons,**” *Physica B: Condensed Matter*, 2018. [Online]. Available: <https://doi.org/10.1016/j.physb.2018.01.019>
- [3] U. Rucker, T. Cronert, J. Voigt, J. Dabruck, P.-E. Doege, J. Ulrich, R. Nabbi, Y. Beßler, M. Butzek, M. Büscher *et al.*, “**The Jülich high-brilliance neutron source project,**” *The European Physical Journal Plus*, vol. 131, no. 1, p. 19, 2016. [Online]. Available: <https://doi.org/10.1140/epjp/i2016-16019-5>
- [4] B. V. Vasiliev, “**Some Problems of Elementary Particles Physics and Gilbert’s Postulate,**” *Journal of Modern Physics*, vol. 7, no. 14, p. 1874, 2016.
- [5] J. Beringer *et al.*, “**Review of Particle Physics,**” *Phys. Rev. D*, vol. 86, no. 1, p. 010001, Jul. 2012.
- [6] H. Dehmelt, “**A Single Atomic Particle Forever Floating at Rest in Free Space: New Value for Electron Radius,**” *Physica Scripta*, vol. T22, pp. 102–110, Jan 1988. [Online]. Available: <https://doi.org/10.1088%2F0031-8949%2F1988%2Ft22%2F016>
- [7] N. Colonna, F. Gunsing, and F. Käppeler, “**Neutron physics with accelerators,**” *Progress in Particle and Nuclear Physics*, vol. 101, pp. 177–203, 2018. [Online]. Available: <https://doi.org/10.1016/j.pnpnp.2018.02.002>
- [8] R. Winter, “**Condensed Matter Physics [image],**” Nov 2017. [Online]. Available: <http://users.aber.ac.uk/ruw/teach/334/scatterth.php>
- [9] M. M. Castellanos, A. McAuley, and J. E. Curtis, “**Investigating structure and dynamics of proteins in amorphous phases using neutron scattering,**” *Computational and*

- structural biotechnology journal*, vol. 15, pp. 117–130, 2017. [Online]. Available: <https://doi.org/10.1016/j.csbj.2016.12.004>
- [10] M. Strobl, I. Manke, N. Kardjilov, A. Hilger, M. Dawson, and J. Banhart, “**Advances in neutron radiography and tomography**,” *Journal of Physics D: Applied Physics*, vol. 42, no. 24, p. 243001, 2009. [Online]. Available: [stacks.iop.org/JPhysD/42/243001](https://stacks.iop.org/JPhysD/42/243001)
- [11] I. RADIA and Y. Rep, “**Neutron Generators for Analytical Purposes**,” *IAEA radiation technology reports series, ISSN*, pp. 2225–8833, 2012. [Online]. Available: <https://www.ipen.br/biblioteca/slr/cel/0113.pdf>
- [12] D. Habs and U. Köster, “**Production of medical radioisotopes with high specific activity in photonuclear reactions with  $\gamma$ -beams of high intensity and large brilliance**,” *Applied Physics B*, vol. 103, no. 2, pp. 501–519, May 2011. [Online]. Available: <https://doi.org/10.1007/s00340-010-4278-1>
- [13] S. Banerjee, M. R. A. Pillai, and N. Ramamoorthy, “**Evolution of Tc-99m in diagnostic radiopharmaceuticals**,” in *Seminars in nuclear medicine*, vol. 31, no. 4. Elsevier, 2001, pp. 260–277. [Online]. Available: <https://doi.org/10.1053/snuc.2001.26205>
- [14] IAEA, in *Non-HEU Production Technologies for Molybdenum-99 and Technetium-99m*, ser. IAEA Nuclear Energy Series. Vienna, Austria: International Atomic Energy Agency, 2013, no. NFT-5.4.
- [15] F. R. Knapp, S. Mirzadeh, and A. Beets, “**Reactor production and processing of therapeutic radioisotopes for applications in nuclear medicine**,” *Journal of radioanalytical and nuclear chemistry*, vol. 205, no. 1, pp. 93–100, 1996. [Online]. Available: <https://doi.org/10.1007/BF02040554>
- [16] K. Nedunchezian, N. Aswath, M. Thiruppathy, and S. Thirugnanamurthy, “**Boron neutron capture therapy-a literature review**,” *Journal of clinical and diagnostic research: JCDR*, vol. 10, no. 12, p. ZE01, 2016. [Online]. Available: <https://www.ncbi.nlm.nih.gov/pmc/articles/PMC5296588/pdf/jcdr-10-ZE01.pdf>
- [17] “**Nuclear Technology Review 2008**,” IAEA, Tech. Rep., GC(52)/INF/3 (2008).
- [18] I. F. R. C. (IFRC), “**Status report on fusion research**,” *Nuclear Fusion*, vol. 45, no. 10A, pp. A1–A28, sep 2005. [Online]. Available: <https://doi.org/10.1088%2F0029-5515%2F45%2F10a%2F001>
- [19] J. Wesson and D. J. Campbell, *Tokamaks*. Oxford university press, 2011, vol. 149.
- [20] A. Coc, J.-P. Uzan, and E. Vangioni, “**Standard big bang nucleosynthesis and primordial CNO abundances after Planck**,” *Journal of Cosmology and Astroparticle Physics*, vol. 2014, no. 10, pp. 050–050, oct 2014. [Online]. Available: <https://doi.org/10.1088%2F1475-7516%2F2014%2F10%2F050>

- [21] G. Wallerstein, I. Iben, P. Parker, A. M. Boesgaard, G. M. Hale, A. E. Champagne, C. A. Barnes, F. Käppeler, V. V. Smith, R. D. Hoffman, F. X. Timmes, C. Sneden, R. N. Boyd, B. S. Meyer, and D. L. Lambert, “**Synthesis of the elements in stars: forty years of progress,**” *Rev. Mod. Phys.*, vol. 69, pp. 995–1084, Oct 1997. [Online]. Available: <https://link.aps.org/doi/10.1103/RevModPhys.69.995>
- [22] F. Käppeler, R. Gallino, S. Bisterzo, and W. Aoki, “**The s process: Nuclear physics, stellar models, and observations,**” *Rev. Mod. Phys.*, vol. 83, pp. 157–193, Apr 2011. [Online]. Available: <https://link.aps.org/doi/10.1103/RevModPhys.83.157>
- [23] S. E. Woosley, A. Heger, and T. A. Weaver, “**The evolution and explosion of massive stars,**” *Rev. Mod. Phys.*, vol. 74, pp. 1015–1071, Nov 2002. [Online]. Available: <https://link.aps.org/doi/10.1103/RevModPhys.74.1015>
- [24] C. Freiburghaus, S. Rosswog, and F.-K. Thielemann, “**r-process in neutron star mergers,**” *The Astrophysical Journal*, vol. 525, no. 2, pp. L121–L124, nov 1999. [Online]. Available: <https://doi.org/10.1086%2F312343>
- [25] I. Anderson, C. Andreani, J. Carpenter, G. Festa, G. Gorini, C.-K. Loong, and R. Senesi, “**Research opportunities with compact accelerator-driven neutron sources,**” *Physics Reports*, vol. 654, pp. 1–58, 2016. [Online]. Available: <https://doi.org/10.1016/j.physrep.2016.07.007>
- [26] F. J. Bermejo and F. Sordo, “**Chapter 2 - Neutron Sources,**” in *Neutron Scattering – Fundamentals*, ser. Experimental Methods in the Physical Sciences, F. Fernandez-Alonso and D. L. Price, Eds. Academic Press, 2013, vol. 44, pp. 137 – 243. [Online]. Available: <https://doi.org/10.1016/B978-0-12-398374-9.00002-4>
- [27] J. Müller and T. Cronert, “**Die Neutronenlandschaft in Europa** [image],” April 2016. [Online]. Available: [http://scienceblogs.de/nucular/files/2016/02/pyramide\\_mittel.jpg](http://scienceblogs.de/nucular/files/2016/02/pyramide_mittel.jpg)
- [28] J. Müller and T. Cronert, “**Ein Bild zur Rettung der europäischen Neutronenlandschaft** [image],” Sept 2017. [Online]. Available: [http://scienceblogs.de/nucular/files/2017/09/Pyramide\\_pos\\_V02.jpg](http://scienceblogs.de/nucular/files/2017/09/Pyramide_pos_V02.jpg)
- [29] D. Mills, J. Helliwell, Å. Kvik, T. Ohta, I. Robinson, and A. Authier, “**Report of the Working Group on Synchrotron Radiation Nomenclature—brightness, spectral brightness or brilliance?**” *Journal of synchrotron radiation*, vol. 12, no. 3, pp. 385–385, 2005. [Online]. Available: <https://doi.org/10.1107/S090904950500796X>
- [30] P. Zakalek, T. Cronert, J. Baggemann, P.-E. Doege, M. Rimmler, J. Voigt, E. Mauerhofer, U. Rücker, and T. Brückel, “**High Brilliance Neutron Source Project,**” *under Publication*.
- [31] E. Mauerhofer *et al.*, “**Conceptual Design Report, NOVA ERA (Neutrons Obtained Via Accelerator for Education and Research Activities), A Jülich High Brilliance Neutron Source Project,**” Jülich Center for Neutron Science, Forschungszentrum Jülich GmbH, Tech. Rep., 2017.

- [32] “**Development opportunities for small and medium scale accelerator driven neutron sources,**” IAEA, Tech. Rep., IAEA-TECDOC-1439 (2005).
- [33] G. Mank, G. Bauer, and F. Mulhauser, “**Accelerators for neutron generation and their applications,**” *Reviews Of Accelerator Science And Technology: Volume 4: Accelerator Applications in Industry and the Environment*, pp. 219–233, 2011.
- [34] P. Zakalek, P.-E. Doege, J. Baggemann, T. Cronert, Y. Beßler, M. Butzek, J. Wolters, E. Mauerhofer, U. Rucker, T. Gutberlet *et al.*, “**Temperature profiles inside a target irradiated with protons or deuterons for the development of a compact accelerator driven neutron source,**” *Physica B: Condensed Matter*, vol. 551, pp. 484–487, 2018. [Online]. Available: <https://doi.org/10.1016/j.physb.2018.01.049>
- [35] T. Rinckel, D. Baxter, J. Doskow, P. Sokol, and T. Todd, “**Target performance at the low energy neutron source,**” *Physics Procedia*, vol. 26, pp. 168–177, 2012. [Online]. Available: <https://doi.org/10.1016/j.phpro.2012.03.022>
- [36] P.-E. Doege, P. Zakalek, J. Baggemann, E. Mauerhofer, U. Rucker, T. Cronert, T. Gutberlet, Y. Beßler, J. Wolters, M. Butzek *et al.*, “**Parametric study and design improvements for the target of NOVA ERA,**” *Journal of Neutron Research*, no. Preprint, pp. 1–8, 2018. [Online]. Available: <https://doi.org/10.3233/JNR-180064>
- [37] J. P. Biersack and L. Haggmark, “**A Monte Carlo computer program for the transport of energetic ions in amorphous targets,**” *Nuclear Instruments and Methods*, vol. 174, no. 1-2, pp. 257–269, 1980. [Online]. Available: [https://doi.org/10.1016/0029-554X\(80\)90440-1](https://doi.org/10.1016/0029-554X(80)90440-1)
- [38] P. E. Hodgson, E. Gadioli, and E. Gadioli-Erba, *Introductory nuclear physics*. Oxford Univ. Press, 1997. [Online]. Available: <http://cds.cern.ch/record/365577>
- [39] M. Chadwick, P. Obložinský, M. Herman, N. Greene, R. McKnight, D. Smith, P. Young, R. MacFarlane, G. Hale, S. Frankle *et al.*, “**ENDF/B-VII. 0: next generation evaluated nuclear data library for nuclear science and technology,**” *Nuclear data sheets*, vol. 107, no. 12, pp. 2931–3060, 2006. [Online]. Available: <https://doi.org/10.1016/j.nds.2006.11.001>
- [40] N. Otuka, E. Dupont, V. Semkova, B. Pritychenko, A. Blokhin, M. Aikawa, S. Babykina, M. Bossant, G. Chen, S. Dunaeva *et al.*, “**Towards a more complete and accurate experimental nuclear reaction data library (EXFOR): international collaboration between nuclear reaction data centres (NRDC),**” *Nuclear Data Sheets*, vol. 120, pp. 272–276, 2014. [Online]. Available: <https://doi.org/10.1016/j.nds.2014.07.065>
- [41] C. A. Bertulani, “**Nuclear Reactions,**” *Wiley Encyclopedia of Physics*, Aug 2009. [Online]. Available: <https://arxiv.org/pdf/0908.3275.pdf>
- [42] C. Rossi Alvarez *et al.*, “**Challenges in the modeling of nuclear reactions for theranostic applications,**” *CERN Proc.*, vol. 1, pp. 349–354, 2019. [Online]. Available: <http://cds.cern.ch/record/2669510>

- [43] J. C. Overley, “**Nuclear Reactions And Scattering**,” *Salem Press Encyclopedia of Science*, vol. Jg. 2018-06-30, 2018.
- [44] J. Cugnon and P. Henrotte, “**Nuclear Reactions Mechanisms: from Compound Nucleus to Multiple Scattering**,” Université de Louvain-la-Neuve, Tech. Rep., 2002. [Online]. Available: <https://orbi.uliege.be/bitstream/2268/211386/1/177.pdf>
- [45] TENDL-2017, “**TALYS-based evaluated nuclear data library [protons]**,” 2017. [Online]. Available: [https://tendl.web.psi.ch/tendl\\_2017/proton\\_html/Be/ProtonBe09xs.html](https://tendl.web.psi.ch/tendl_2017/proton_html/Be/ProtonBe09xs.html)
- [46] —, “**TALYS-based evaluated nuclear data library [deuterons]**,” 2017. [Online]. Available: [https://tendl.web.psi.ch/tendl\\_2017/deuteron\\_html/Be/DeuteronBe09xs.html](https://tendl.web.psi.ch/tendl_2017/deuteron_html/Be/DeuteronBe09xs.html)
- [47] S. Weinberg, “**A model of leptons**,” *Physical review letters*, vol. 19, no. 21, p. 1264, 1967. [Online]. Available: <https://doi.org/10.1103/PhysRevLett.19.1264>
- [48] J. Lilley, *Nuclear physics: principles and applications*. John Wiley & Sons, 2013.
- [49] G. F. Knoll, *Radiation detection and measurement*. John Wiley & Sons, 2010.
- [50] H. Gümüş, “**New stopping power formula for intermediate energy electrons**,” *Applied Radiation and Isotopes*, vol. 66, no. 12, pp. 1886–1890, 2008. [Online]. Available: <https://doi.org/10.1016/j.apradiso.2008.05.006>
- [51] J. I. Goldstein, D. E. Newbury, J. R. Michael, N. W. Ritchie, J. H. J. Scott, and D. C. Joy, *Scanning electron microscopy and X-ray microanalysis*. Springer, 2017.
- [52] K. Kanaya and S. Okayama, “**Penetration and energy-loss theory of electrons in solid targets**,” *Journal of Physics D: Applied Physics*, vol. 5, no. 1, p. 43, 1972. [Online]. Available: <https://doi.org/10.1088/0022-3727/5/1/308>
- [53] P. Hovington, D. Drouin, and R. Gauvin, “**CASINO: A new Monte Carlo code in C language for electron beam interaction—Part I: Description of the program**,” *Scanning*, vol. 19, no. 1, pp. 1–14, 1997. [Online]. Available: <https://doi.org/10.1002/sca.4950190101>
- [54] D. Drouin, A. R. Couture, D. Joly, X. Tastet, V. Aimez, and R. Gauvin, “**CASINO V2. 42—a fast and easy-to-use modeling tool for scanning electron microscopy and microanalysis users**,” *Scanning: The Journal of Scanning Microscopies*, vol. 29, no. 3, pp. 92–101, 2007. [Online]. Available: <https://doi.org/10.1002/sca.20000>
- [55] F. Salvat, J. M. Fernández-Varea, and J. Sempau, “**PENELOPE-2008: A code system for Monte Carlo simulation of electron and photon transport**,” in *Workshop Proceedings*, vol. 4, no. 6222, 2006, p. 7.
- [56] C. R. Sundararajan, *Probabilistic structural mechanics handbook: theory and industrial applications*. Springer Science & Business Media, 2012.
- [57] Z. M. Zhang, B. K. Tsai, and G. Machin, *Radiometric temperature measurements: I. Fundamentals*. Academic press, 2009, vol. 42.

- 
- [58] J. Meseguer, I. Pérez-Grande, and A. Sanz-Andrés, *Spacecraft thermal control*. Elsevier, 2012, ch. 5, pp. 73–86.
- [59] X. Dérobert, J.-P. Balayssac, Z. M. Sbartai, and J. Dumoulin, *Non-destructive testing and evaluation of civil engineering structures*. Elsevier, 2017, ch. 3, pp. 87–134.
- [60] O. Breitenstein, W. Warta, M. C. Schubert, and M. Langenkamp, *Lock-in thermography: Basics and use for evaluating electronic devices and materials*. Springer, 2018, vol. 10, ch. 2, pp. 7–51.
- [61] R. Pogge, “**Infrared Absorption of the Atmosphere from 1-28 microns** [image],” 2019. [Online]. Available: [http://www.astronomy.ohio-state.edu/~pogge/Ast161/Unit5/Images/atmos\\_mirtran.png](http://www.astronomy.ohio-state.edu/~pogge/Ast161/Unit5/Images/atmos_mirtran.png)
- [62] Space Research Institute of the Russian Academy of Sciences, “**Black-body radiation** [pdf],” 2019. [Online]. Available: [http://www.iki.rssi.ru/asp/pub\\_sha1/Sharch06.pdf](http://www.iki.rssi.ru/asp/pub_sha1/Sharch06.pdf)
- [63] V. I. Sapritsky, “**Black-body radiometry**,” *Metrologia*, vol. 32, no. 6, pp. 411–417, Dec 1995. [Online]. Available: <https://doi.org/10.1088%2F0026-1394%2F32%2F6%2F2>
- [64] G. K. Burgess and R. G. Waltenberg, *The emissivity of metals and oxides*. US Government Printing Office, 1915.
- [65] S. Lecheler, *Numerische Strömungsberechnung*. Springer, 2009.
- [66] Various Authors, “**ITER Materials Properties Handbook (MPH)**, ITER Doc. G 74 MA 16 04-05-07 R0.1,” ITER, Tech. Rep.
- [67] DIAS Infrared Systems, “**PYROSPOT DPE 10M/DPE 10MV** [pdf],” 2018. [Online]. Available: [http://www.dias-infrared.de/pdf/pyrospot\\_dpe10m\\_dpe10mv\\_eng\\_mail.pdf](http://www.dias-infrared.de/pdf/pyrospot_dpe10m_dpe10mv_eng_mail.pdf)